Moisture balance over the Iberian Peninsula according to a regional climate model: The impact of 3DVAR data assimilation.

Santos J. González-Rojí[1]*, Jon Sáenz[1,2], Gabriel Ibarra-Berastegi[2,3] and Javier Díaz de Argandoña[4].

[1]Applied Physics II Department, University of the Basque Country UPV/EHU, Leioa, Bizkaia, Spain.
[2]Joint Research Unit BEGIK, Spanish Oceanographic Institute-University of the Basque Country, Plentziako Itsas Estazioa. University of the Basque Country UPV/EHU, Plentzia, Bizkaia, Spain.
[3]Fluid Mechanics & N.I. Department, University of the Basque Country UPV/EHU, Bilbao, Bizkaia, Spain
[4]Applied Physics I Department, University of the Basque Country UPV/EHU, Vitoria-Gazteiz, Araba, Spain

Key Points:

- The simulation using 3DVAR data assimilation (D) improves the results obtained using the high resolution model alone (N).
- The simulation using 3DVAR data assimilation produces better or comparable results to ERAI for precipitation, IWV and evaporation.

*Faculty of Science and Technology, Barrio Sarriena, s/n, 48940 Leioa, Bizkaia

Corresponding author: Santos J. González-Rojí, santosjose.gonzalez@ehu.eus

Abstract
An analysis of the atmospheric branch of the hydrological cycle by means of a 15 km resolution numerical integration performed using WRF nested in ERA Interim is presented. Two WRF experiments covering the period 2010-2014 were prepared. The first one (N) was configured as in standard numerical downscaling experiments. The second one (D), with the same parameterizations, included a step of 3DVAR data assimilation every six hours. Apart from comparing our results with ERA Interim data, several observational datasets were used to validate the precipitable water (radiosondes and MODIS data), precipitation (EOBS, ECA&D, TRMM and GPCP) or evaporation (GLEAM). The verification results showed that the D experiment systematically performs better than N and in many instances, too, better than the forcing reanalysis. According to the results, the leading terms of the water balance are the tendency of the precipitable water, the divergence of moisture flux, evaporation and precipitation. No spatial patterns were recognizable for the annual accumulated evaporation, but the effect of the Atlantic fronts was detected in the precipitation patterns. The transboundary moisture fluxes through the contour of the Iberian Peninsula behave differently depending on the season during 2010-2014. During winter, they show a net moisture import through the boundaries. During spring, summer or autumn moisture is exported specially through the Mediterranean coast, and only during midday this feature is reversed due to sea breezes.

This paper is a postprint version of *S. J. González-Rojí, J. Sáenz, G. Ibarra-Berastegi, J. Díaz-Argandoña (2018), Moisture balance over the Iberian Peninsula according to a regional climate model: The impact of 3DVAR data assimilation. Journal of Geophysical Research-Atmospheres, doi: 10.1002/2017JD027511*

1 Introduction

The Iberian Peninsula (hereafter, IP) is an interesting place to carry out studies on the atmospheric branch of the regional hydrologic cycle. Surrounded by the Atlantic ocean and the Mediterranean sea, the IP is influenced by large-scale moisture transports [*Fernández et al.*, 2003; *Gimeno et al.*, 2010; *Gómez-Hernández et al.*, 2013]. The atmospheric circulation in this region is strongly influenced by teleconnection patterns affecting the North Atlantic area [*Rodríguez-Puebla et al.*, 2001], such as the North Atlantic Oscillation (NAO) [*Haylock and Goodess*, 2004; *Zveryaev et al.*, 2008] or the East Atlantic (EA) [*Rodríguez-Puebla et al.*, 1998; *Sáenz et al.*, 2001; *Zveryaev et al.*, 2008] and blockings [*Sousa et al.*, 2017].

The aforementioned large-scale factors interact with the Iberian steep topography which delimits different climatic regions. Three big climatic areas can be observed in the IP according to recent climate classifications [*Kottek et al.*, 2006; *Peel et al.*, 2007; *Lionello et al.*, 2012; *Rubel et al.*, 2017]: Arid (B group), Warm Temperature (C group) and Snow Climates (D group). Over the IP, the second climate can be divided into two subgroups depending on its dry or humid seasons (Cs and Cf). Therefore, four areas can be found: (1) Semiarid and Arid climate, in the south of the IP. (2) Mediterranean, in the southwestern IP. (3) Oceanic, located mainly in the north of Spain and Portugal. Finally, (4) Alpine climate, in mountain ranges such as the Pyreness, Picos de Europa or Sierra Nevada.

The effects of the climatic areas and the atmospheric circulation determine the precipitation and the vertically integrated water column (integrated water vapour, IWV) in the IP. The spatial patterns of precipitation change during the year: the north and the west are affected particularly during winter, but for the south and the east the most important season is autumn [*Rodríguez-Puebla et al.*, 1998; *Romero et al.*, 1999; *Esteban-Parra et al.*, 1998a]. The amount of precipitation in the centre of the IP is larger during the early spring, which is in accordance to *Tullot* [2000]. Nowadays a decrease in the amount of precipitation has been observed [*Rodríguez-Puebla et al.*, 1998; *Paredes et al.*, 2006], not only in the IP but

also in the entire Mediterranean basin [*Trigo et al.*, 1999; *Quadrelli et al.*, 2001]. Additional analyses extend the study of moisture variations to fields such as relative or specific humidities [*Vicente-Serrano et al.*, 2014], showing a decrease in relative humidity but not a similar change in specific humidity over the IP.

The variability of the IWV during the year also depends on the region. According to *Zveryaev et al.* [2008], a strong variability over the IP is observed during winter, with large values near the oceanic or marine regions. During summer, the largest values are located near the Mediterranean sea. In addition, *Ortiz de Galisteo et al.* [2011] suggested that local effects (e.g. breezes) modify the diurnal cycle of IWV, especially during summer.

Studies of the precipitation and IWV are part of an integrated assessment of the water balance over a region. During the last decades, a growing number of studies on this topic has been made [*Gutowski Jr. et al.*, 1997; *Trenberth and Guillemot*, 1998; *Berbery and Rasmusson*, 1999; *Trenberth et al.*, 2007; *Yeh and Famiglietti*, 2008]. Many of these studies focus on different regions, applying different methodologies. Focusing over the IP *Vérant et al.* [2004] analysed the effect of the spatial resolution of regional simulations for terrestrial water balance.

Nowadays, it is commonly accepted that a dynamical model nested within a Global Climate Model (GCM) can provide more accurate simulated fields than the GCM itself [*Jones et al.*, 1995; *Foley*, 2010; *Rummukainen*, 2010; *Feser et al.*, 2011; *Önol*, 2012]. In addition, even if the regional models are fed only by boundary conditions, they are able to reproduce the small-scale features dependent on the resolution of the surface of the domain such as orographic precipitation and fast-floods [*Rockel et al.*, 2008; *Leung and Qian*, 2009]. However, regional coupled ocean-atmosphere models can be sensitive to the domain in regions where this coupling is important, as suggested by *Sein et al.* [2014] when downscaling for the Artic region. In terms of regional models, the Weather Research and Forecasting Model (WRF, ARW) [*Skamarock et al.*, 2008] has been applied in the study of daily precipitation [*Cardoso et al.*, 2013] at different horizontal resolutions. On the other hand, the relationship between evapotranspiration and the maximum of precipitation in spring in the IP was analysed using WRF [*Rios-Entenza et al.*, 2014; *Eiras-Barca et al.*, 2016] and also in the analysis of moisture recycling [*Rios-Entenza et al.*, 2014]. An ensemble of regional models taking part in the EURO-CORDEX initiative was analysed to identify impacts on temperature and precipitation indices by future climate change over Europe [*Dosio*, 2016], Portugal [*Soares et al.*, 2015] or Spain [*Domínguez et al.*, 2013]. These studies have already shown that regional climate models are useful tools in the analysis of precipitation over the area. They have also shown that the WRF model is widely used, but most of the times without including the data assimilation step on it.

Focusing on the Iberian peninsula, the number of studies including the data assimilation step in their regional simulations is very small. The most similar study to ours that has been found in the bibliography is the numerical weather prediction carried out operationally at the Spanish Meteorological Agency (AEMET) using the HIRLAM model [*Navascués et al.*, 2013]. In this case, the 3DVAR data assimilation scheme is run every six hours, showing a positive impact in the forecast quality. However, it does not include a comparison between a simulation with the same configuration but without the 3DVAR data assimilation step.

Our main objective is to extend the previous studies to a full analysis of the whole atmospheric branch of the water cycle over the Iberian Peninsula. In particular, an evaluation of the advantage of the use of a 3DVAR assimilation step during the runs with the regional climate model in the closure of the moisture balance will be assessed. To that extent, the ability of numerical experiments carried out using WRF covering the period 2010-2014 will be checked. As those simulations are not long enough to address neither the climatology nor the interannual variability, these topics will not be studied. Two simulations were carried out with WRF: one of them (experiment D) included 3DVAR data assimilation every six hours,

and the second one (N) was configured so that, after initialization, only the boundary conditions drive the model. The water balance simulated by both runs was analysed. First, the balance was internally checked (according to the model results) to identify the consistency of the fields. Additionally, the model results were also checked by comparing them with observational datasets (particularly IWV, precipitation and evaporation). Finally, a comparison of both experiments provided further insight into the benefits of applying the assimilation of observations while running WRF. It is shown that the resulting products improve the spatial resolution compared to ERA Interim (ERAI) [*Dee et al.*, 2011]. The analyses also outperform the verification fields from the forcing reanalysis, thus adding value to it.

This paper is organised in five main sections. In section two, the configuration of the WRF model is described along with the characteristics of the different datasets used for validation of the elements of the water balance. A brief outline of the techniques used for comparing the datasets is also presented in that section. In section three, the water balance results for the IP during the period 2010-2014 are presented, along with the validation of IWV, precipitation and evaporation. A discussion about the key findings emerging from the study, and concluding remarks about our research are presented in sections four and five respectively.

2 Data and Methods

2.1 WRF Model Set-up

The WRF model (version 3.6.1) nested inside ERAI was used to create two different simulations spanning the period 2010-2014. The runs were started in 2009. The first year (2009) was used as spin-up for the land surface model and not analysed, as done in previous studies [*Argüeso et al.*, 2011; *Zheng et al.*, 2017]. Boundary conditions from ERAI are provided every 6-hours at 0.75 degrees resolution and with 20 vertical levels (from 5 hPa to 1000 hPa). Boundary conditions drive the model after the initialization in the first experiment (N). The second experiment (D) is configured exactly the same way as N, but 3DVAR data assimilation [*Barker et al.*, 2012] is run every six hours (at 00 UTC, 06 UTC, 12 UTC and 18 UTC) using observations from the NCEP ADP Global Upper Air and Surface Weather Observations (PREPBUFR dataset). Observations included inside a 120-minute window centered at these analysis times are used for the 3DVAR analysis. High-resolution ($0.25° \times 0.25°$) daily sea surface temperature (SST) fields from NOAA OI SST v2 [*Reynolds et al.*, 2007] were included in both simulations.

The domain is centered on the IP but it also covers much of north-western Africa and western Europe (20°-60°N, 25°W-15°E) (Figure 19). A mask over the IP (coloured in red in Figure 19) was defined in order to select the points that were included in the analysis of the water balance. Both simulations used 51 vertical levels and 15x15 km^2 horizontal resolution. With this resolution, the WRF model is able to better follow the topography of the IP than ERA Interim. Figure 19 (bottom) shows the topography according to GLOBE dataset (1 km resolution; [*Hastings and Dunbar*, 1999]) and that from WRF. Besides the NOAH Land Surface Model mentioned above, some other parametrizations were used such as WRF five class microphysics, MYNN2 Planetary Boundary Layer scheme, RRTMG scheme for both short-wave and long-wave radiation and Tiedtke scheme for cumulus convection.

The background error covariance matrices were adapted to the region and the physical parameterizations used in the D experiment by means of the CV5 in WRFDA [*Parrish and Derber*, 1992] by creating a 13-month long run from January 2007 until February 2008. The background error covariances vary monthly and were always built using 90 days around the corresponding month. Integrations used during this 90 day period were initialized either at 00 UTC or at 12 UTC in order to properly sample day and night. For example, the background error covariance matrix for January was created using the data from December to February and so on for the rest of the monthly varying background error covariance matrices.

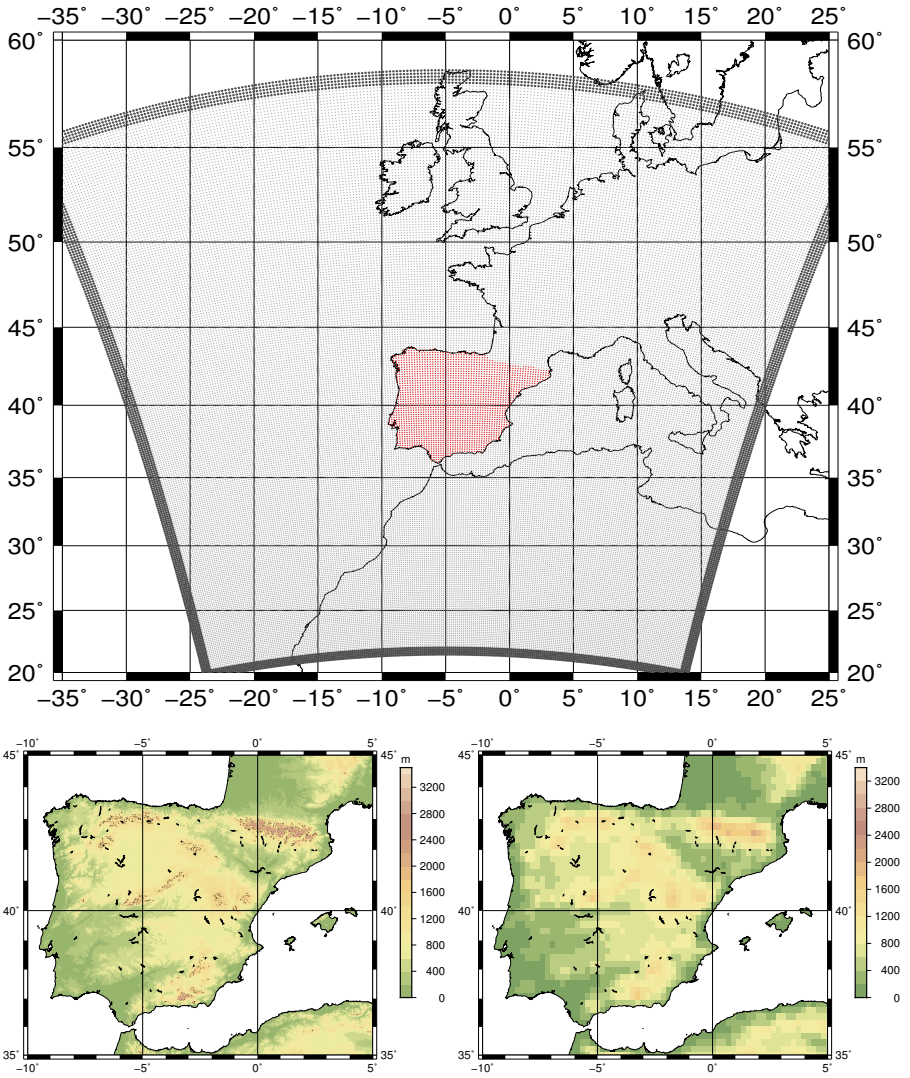

Figure 1. Top: Domain of both simulations marked with grey dots. The mask defined for the IP is plotted in red. That was the area used for verification. Bottom left: topography of the IP taken from GLOBE dataset (at 1 km resolution; [*Hastings and Dunbar*, 1999]) and bottom right: topography as represented in our WRF simulations (15 km resolution).

The first experiment (N) is created by running 6-hour long segments that are restarted from the restart file produced by the previous segment. Thus, this methodology is equivalent to a continuous WRF run where boundary conditions feed the model every 6-hours after the initialization of the model in January 1st, 2009. On the other hand, the data assimilation experiment (D) is run during 12 hours starting from every analysis (00 UTC, 06 UTC, 12 UTC and 18 UTC). For this simulation, there is only a cold start in January 1st, 2009. The analyses are produced by using the output from the model at a six-hour forecast step from the previous segment as first guess in a 3DVAR data assimilation scheme where observations from PREPBUFR files are used. The outputs of both simulations are saved every three hours, which means that analysis from the D experiment and 3-hour forecasts (03 UTC, 09 UTC, 15 UTC and 21 UTC) are included in our results. The same recording frequency for outputs is used for the continuous N WRF run.

2.2 Validation Datasets

In order to independently validate each element of the water balance, several datasets were used. The number of available datasets is not very high because at the same time they must cover the period 2010-2014 and they must ideally have a comparable resolution to that used in the model runs.

In order to validate the simulated precipitable water (IWV), atmospheric radiosondes and Moderate Resolution Imaging Spectroradiometer (MODIS) data were used [*Gao and Kaufman*, 2003]. The radiosondes were obtained from the server of the University of Wyoming with only eight stations being available for the IP. In these stations, data are collected twice per day (at 00 UTC and 12 UTC), except for Lisbon station where it is only available once per day (at 12 UTC). We used the bootstrap technique with resampling to create 1000 time series for the validation of our simulations with the radiosondes, in order to accurately represent sampling errors. IWV from ERAI was also included in the validation, after having the vertical integral computed in ECMWF's original model levels.

Data taken from MODIS was also used for validation purposes. This spectroradiometer is an important instrument aboard the Aqua and Terra satellites. Both satellites collect data every 1 to 2 days in many spectral bands. For our validation, Level-2 IWV from both satellites were combined and used in order to improve the temporal resolution of the dataset. 5 km x 5 km spatial resolution was used in a domain centred over the IP (34°-46°N, 12°W-6°E).

For the validation of precipitation, four datasets were used: the ENSEMBLES OBSERVATIONS (EOBS version 12.0, 0.25° resolution) [*Haylock et al.*, 2008; *van den Besselaar et al.*, 2011], the Tropical Rainfall Measuring Mission (TRMM, 0.25° resolution) [*Wang et al.*, 2014], the Global Precipitation Climatology Project (GPCP, 1° resolution) [*Huffman et al.*, 2001] and the European Climate Assessment & Dataset (ECA&D) [*Klein Tank et al.*, 2002], which contains land station observations. For this last dataset, twenty-one stations evenly spaced over the IP were selected in order to represent the different climatic areas without oversampling over some areas (such as Catalonia) where the density of stations is much higher than in the rest of the IP. In Portugal, Lisbon was the only station providing data during the period 2010-2014. All datasets present a daily temporal resolution, with the exception of TRMM which has a 3-hourly resolution. Data from ERAI and both WRF experiments were aggregated to daily values.

Finally, in order to validate the evaporation, version 3.0 of Global Land Evaporation Amsterdam Model (GLEAM) datasets [*Martens et al.*, 2017; *Miralles et al.*, 2011] were used. This dataset is based on observations such as radiation, air temperature, precipitation, snow water equivalent, vegetation optical depth and surface soil moisture from satellites, reanalysis and other observational fields. Three independent GLEAM datasets were available, but only 2 of them were used: v3.0b and v3.0c. In order to arrive to a fair comparison between WRF and ERAI, GLEAM v3.0a dataset was not included in the validation because ERAI's net radiation and air temperature were used as forcings in it. Both selected versions were driven only by satellite data, but the main difference between them was that v3.0c retrieved vegetation optical depth and surface soil moisture from SMOS-observations. Both datasets cover the same domain (50°N-50°S) using a 0.25° x 0.25° regular grid. Data are available with daily temporal resolution.

The verification indices depend on the observational dataset used. For the validation of IWV in radiosondes, Taylor diagrams were used to plot the standard deviation, root mean squared error (RMSE) and Pearson's correlation (r) of both WRF experiments and ERAI against radiosonde data. For the other datasets, which are not prone to the use of Taylor diagrams, the nearest neighbour to each point at WRF's mask for the IP (2108 points) was calculated in the other grids. Then, the results were plotted in coloured maps that represent r and bias. For the calculation of the transboundary fluxes (only computed for the results of

the D model run), normal vectors were defined at the boundary that encloses the mask that covers IP, so that positive transboundary fluxes represent moisture leaving the IP.

2.3 Analysis of the Water Balance

In order to analyse the water budget over the IP simulated by both WRF simulations and ERAI the moisture conservation equation for vertically integrated quantities and surface fluxes (equation 12.9 from *Peixoto and Oort* [1992]) is used:

$$\frac{\partial W}{\partial t} + \vec{\nabla} \cdot \vec{Q} + \frac{\partial W_c}{\partial t} + \vec{\nabla} \cdot \vec{Q_c} = E - P, \tag{1}$$

where W is the IWV, $\vec{\nabla} \cdot \vec{Q}$ is the divergence of moisture flux, and E and P are the evaporation and precipitation, respectively. The subscript c denotes the terms related to the condensates simulated by the model's microphysical parameterization.

Starting from equation 1, the residual η of the water conservation equation was defined for each grid point as follows:

$$\eta = \frac{\partial W}{\partial t} + \vec{\nabla} \cdot \vec{Q} + \frac{\partial W_c}{\partial t} + \vec{\nabla} \cdot \vec{Q_c} - E + P \tag{2}$$

The most important terms in equation 1 (W, $\vec{\nabla} \cdot \vec{Q}$, E, P) are quantitatively verified against observations, namely precipitable water W (subsection 3.1), precipitation P (subsection 3.2) and evaporation E (subsection 3.3) when observations are available. In other cases (such as is the case for divergence of moisture transports $\vec{\nabla} \cdot \vec{Q}$), the verification has been carried out by checking the closure of the water conservation equation, since direct observations do not exist. The spatial pattern of the residual η was studied for both WRF simulations and ERAI, particularly for the annual and seasonal means. Additionally, annual and seasonal accumulation maps were calculated for each term of the water balance, together with areal mean plots when showing time series of evaporation.

3 Results

3.1 Validation of Integrated Water Vapour

Figure 20 shows the results for the comparison of IWV from both WRF experiments and ERAI with radiosondes. The experiment with data assimilation (D) was the one with the best scores in every station available (r between 0.973 and 0.990). It improved the results of the experiment without data assimilation (r between 0.669 and 0.778), but also those for ERAI (r between 0.857 and 0.963).

Scatterplots between both simulations and ERAI with observations (not shown) showed that the slope obtained from the regression line was really well reproduced by both WRF runs (N: from 0.817 to 0.978, D: from 0.918 to 1.001). Especially for the D experiment, which was able to beat ERAI (from 0.787 to 1.009). However, the bias was larger for the N experiment (between 1.960 mm to 4.092 mm), whilst for D and ERAI the spread of the values was smaller (between -1 mm and 1 mm).

Figure 21 shows the verification results for mixed Level 2 (L2) data measured by MODIS aboard Aqua and Terra satellites. Poor values for the N experiment were observed, particularly in the southern and northwestern IP. The D experiment improved the results obtained for N, being quite similar to those obtained for ERA-Interim. ERAI and the D experiment reached the same area-averaged r (0.66), while for the N experiment the area-averaged r was 0.53. It is clear that the agreement between satellite and model precipitable water is lower than between soundings and model data.

The bias between both WRF simulations and ERAI with MODIS L2 data is presented in Figure 22. The mountain ranges across the IP were clearly recognizable in both WRF simulations. The N experiment presented the poorest results near the final stretch of the Tajo,

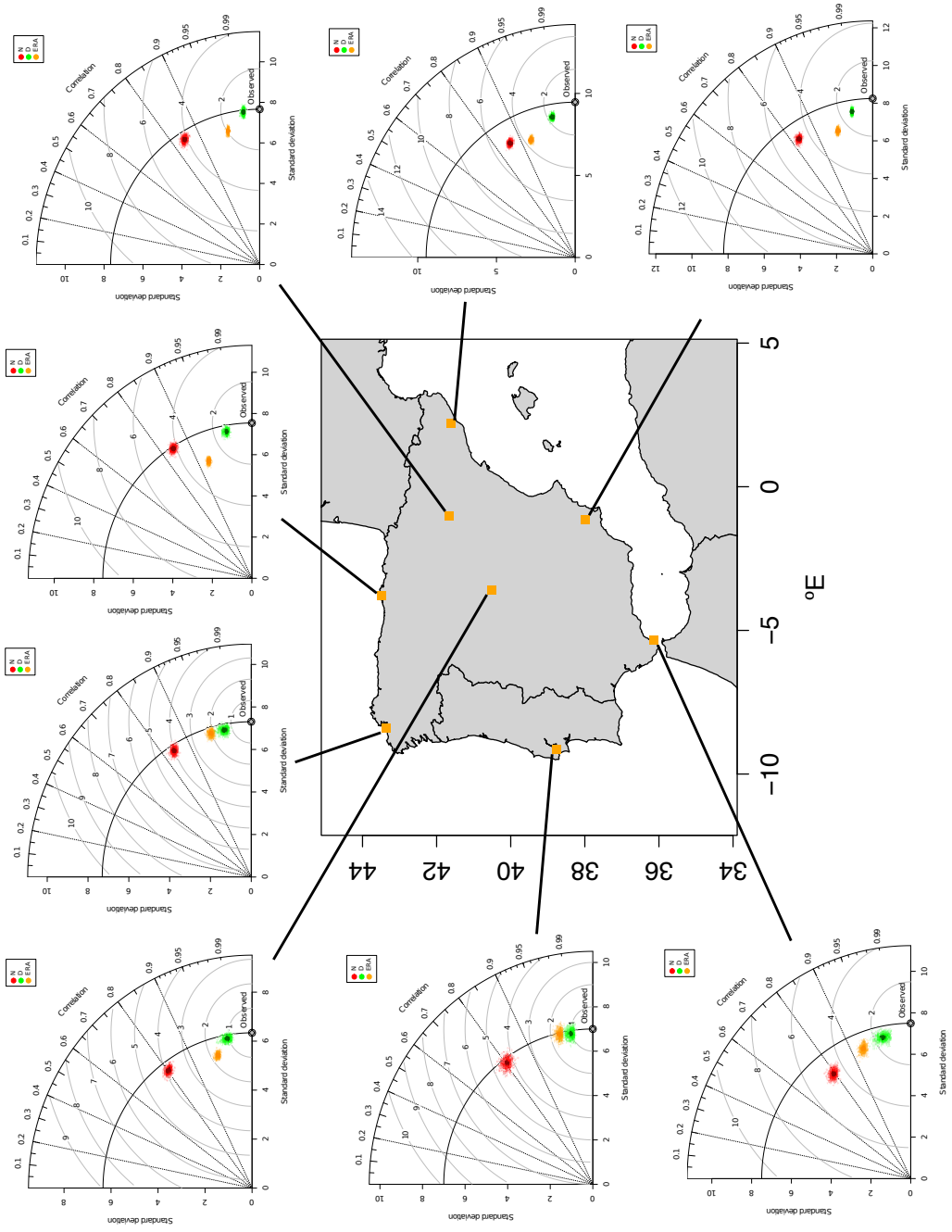

Figure 2. Taylor diagrams showing the standard deviation, r and RMSE results for N and D experiments and ERAI compared to radiosonde data (coloured in red, green and orange respectively). The small dots represent the results for each time series created using the bootstrap technique, while the big dots correspond to the results obtained from the full sample of observed radiosonde data.

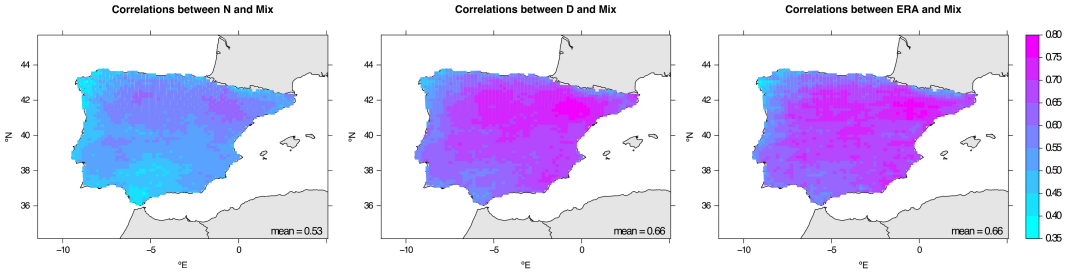

Figure 3. Correlation for both WRF simulations and ERAI compared to IWV data collected by MODIS aboard Aqua and Terra satellites. The spatial average of the points included in the IP is presented in the right bottom corner of the map.

Guadiana and Guadalquivir rivers, but also in the Ebro basin. The D experiment was able to slightly improve these results, reaching similar values to those obtained with ERAI (D: -14.84 mm and ERA: -14.25 mm).

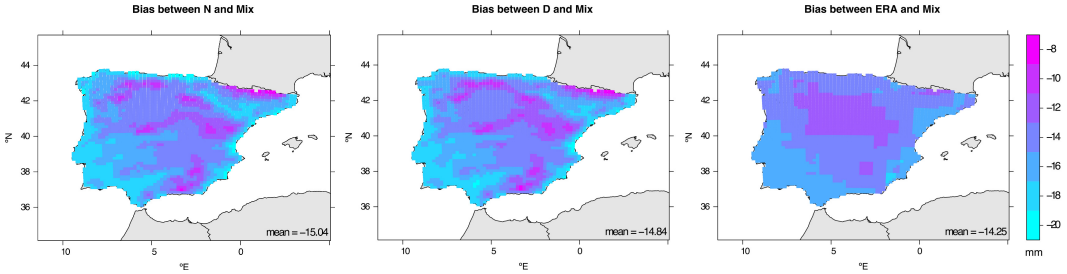

Figure 4. Same as Figure 21, but for bias (mm).

3.2 Validation of Precipitation

Figure 23 shows the results for the comparison of precipitation with EOBS dataset and twenty-one stations from ECA&D. Focusing only on the EOBS results (coloured grid), northwestern IP was well reproduced by the simulations and ERAI. Major problems appear in the southeastern zone, particularly for the N experiment. However, the experiment with data assimilation was able to improve the r in these regions, making it comparable to ERAI as both reach similar areal mean r values: 0.64 and 0.63 respectively.

Focusing on the results from the stations selected from ECA&D, the N experiment obtained the poorest results. Particularly near the Mediterranean coast. The D experiment improved these results in the center and southern regions of Spain (from 0.44 to 0.54). The D experiment also presented better results than ERAI in the south of the IP.

The bias results from EOBS (Figure 24) show large differences for the N experiment in the northwestern part of the IP, The Pyrenees and the Central System. The D experiment shows better agreement, with some discrepancies remaining only in the north of Portugal. A similar pattern is observed for ERAI. Mean biases of 0.07 mm/day and -0.02 mm/day are measured for the D experiment and ERAI respectively.

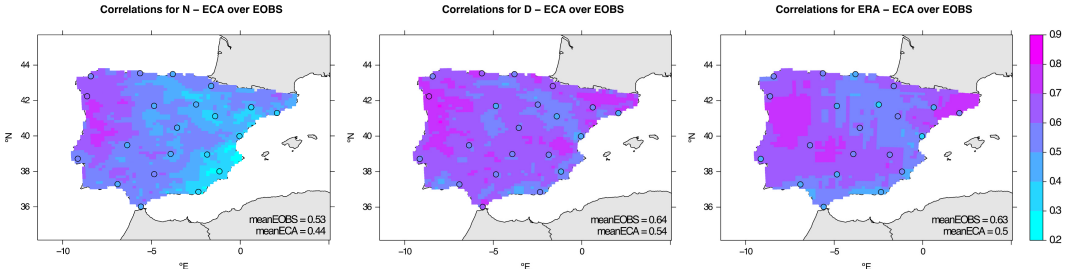

Figure 5. Precipitation correlation maps between EOBS dataset for both WRF simulations and ERA (shaded). Coloured circles represent the correlation of 21 stations selected from ECA&D. The mean r values for EOBS and ECA&D datasets are presented in the right bottom corner of the maps.

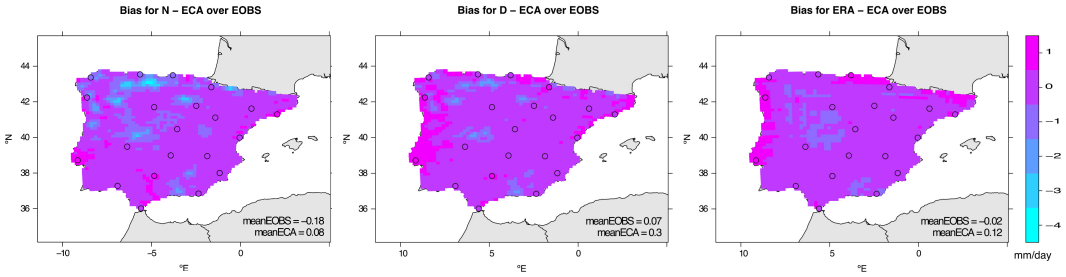

Figure 6. Same as Figure 23, but for bias (mm/day).

According to the results for ECA&D, the biases are better for the inland parts of the IP. In this case, the experiment with data assimilation has the largest mean bias. The N experiment has a mean bias value of 0.08 mm/day, the D experiment 0.3 mm/day and ERAI 0.12 mm/day.

Similar maps are obtained for TRMM and GPCP datasets. They show the southwestern IP region to have poorer r (not shown). In order to summarize the r and bias results for all validation datasets, a quantile-based analysis of the results is presented in Tables 3 and 4. r values for the N experiment were worse than ERA-Interim and the D experiment. The D experiment obtained better (or at least similar) results to those for ERAI in each validation. Highest results for the D experiment were obtained while comparing to EOBS dataset, with values ranging from 0.53 to 0.76 across the IP. Focusing on Table 2, the spread of the values was bigger for the N experiment. Comparable results were observed for ERAI and the D experiment.

3.3 Validation of Evaporation

Analysing the static geographical data used by WRF for our domain, the predominant types of soil and land use over the IP can be studied. The soil type in the region is mainly loam, with the exception of the Guadalquivir Basin that is made of clay. Conversely, the land uses over the IP are more varied. Evergreen and mixed forests are detected in the mountain ranges of the IP. The plateaus are full of croplands, mixed with woody savannas and open scrublands in the southern Spain. A clear relationship with the climatic areas arises from this distribution of land uses. However, three different urban sites can be clearly observed: Barcelona, Madrid and Porto.

These urban points of the grid must be removed since WRF is not able to simulate correctly their evaporation (Figure 25) due to the mismatch between the real land use and the simulated one. The r of these points with their nearest points in GLEAM grid was negative,

Table 1. Spatial quantile-based analysis of the correlations obtained for precipitation in both WRF experiments and ERAI with the validation datasets: EOBS, ECA&D, GPCP and TRMM.

Experiment	**q97.5**	**q95**	**q75.**	**q50**	**q25**	**q5**	**q2.5**
EOBS-N	0.71	0.68	0.59	0.53	0.48	0.36	0.32
EOBS-D	0.76	0.74	0.68	0.64	0.61	0.55	0.53
EOBS-ERA	0.76	0.74	0.68	0.63	0.58	0.52	0.49
ECA&D-N	0.59	0.57	0.49	0.44	0.39	0.31	0.29
ECA&D-D	0.69	0.67	0.57	0.53	0.50	0.46	0.45
ECA&D-ERA	0.60	0.60	0.53	0.50	0.45	0.39	0.38
GPCP-N	0.58	0.57	0.48	0.39	0.31	0.23	0.21
GPCP-D	0.60	0.58	0.53	0.46	0.41	0.32	0.29
GPCP-ERA	0.58	0.58	0.52	0.47	0.41	0.33	0.31
TRMM-N	0.57	0.54	0.44	0.36	0.28	0.20	0.18
TRMM-D	0.63	0.60	0.53	0.48	0.42	0.32	0.30
TRMM-ERA	0.62	0.60	0.55	0.48	0.42	0.35	0.33

Table 2. Same as Table 3 but for bias (mm/day).

Experiment	**q97.5**	**q95**	**q75.**	**q50**	**q25**	**q5**	**q2.5**
EOBS-N	0.59	0.48	0.18	-0.05	-0.39	-1.38	-1.84
EOBS-D	0.88	0.71	0.31	0.12	-0.15	-0.72	-1.05
EOBS-ERA	0.93	0.71	0.16	-0.04	-0.25	-0.59	-0.67
ECA&D-N	0.89	0.68	0.32	0.20	-0.10	-0.90	-0.99
ECA&D-D	1.02	0.77	0.43	0.28	0.09	-0.17	-0.23
ECA&D-ERA	1.09	1.08	0.29	0.00	-0.17	-0.38	-0.42
GPCP-N	1.13	1.06	0.77	0.49	-0.03	-1.42	-2.01
GPCP-D	1.25	1.18	0.87	0.63	0.27	-0.73	-1.19
GPCP-ERA	1.09	0.93	0.63	0.43	0.22	-0.25	-0.55
TRMM-N	0.73	0.51	-0.14	-0.45	-0.88	-2.70	-3.23
TRMM-D	0.86	0.64	-0.05	-0.33	-0.63	-1.81	-2.31
TRMM-ERA	0.90	0.41	-0.21	-0.51	-0.74	-1.66	-1.82

with values between 0 and -0.4. As this was a problem related to the Land Surface Model, all these points were eliminated from the validation.

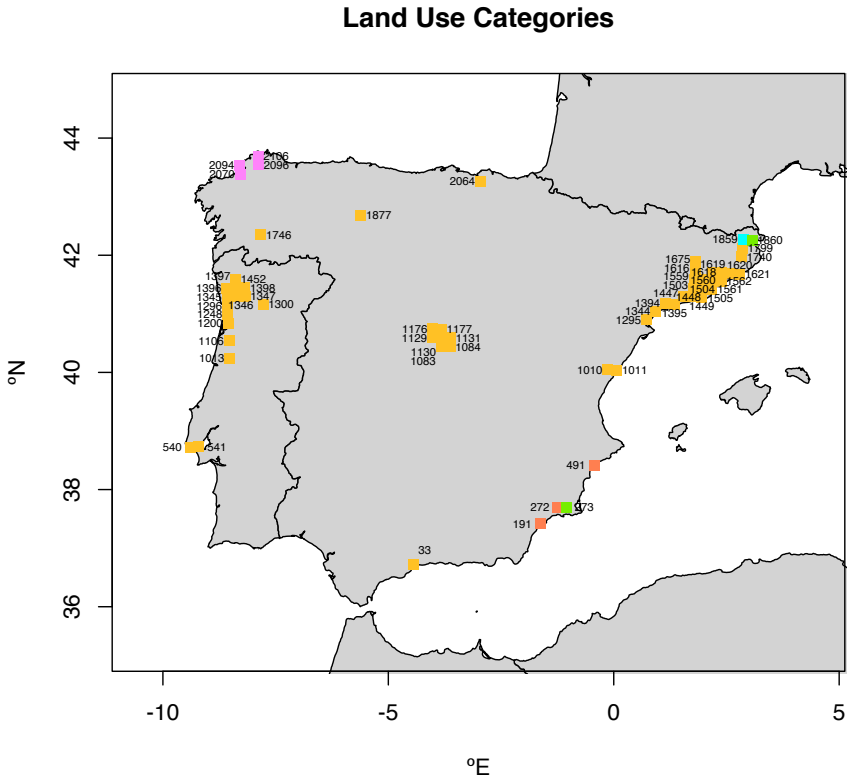

Figure 7. Eliminated points from the validation of evaporation because of the lack of ability to simulate observed evaporation by Noah Land Surface Model depending on their land uses. All urban and built-up grid points (orange) were deleted, but also some points representing evergreen broadleaf forest (magenta), mixed forests (cyan), open shrublands (coral) and croplands (green).

The most remarkable differences between GLEAM 3.0b and 3.0c (for 2011-2014) are concentrated in the north-western and eastern sides of the IP. The highest values of the difference were located in this last region, reaching 0.20 mm/day. Figure 26 shows the r map for the comparison of evaporation with GLEAM v3.0b. For the N experiment, poor results appear near the Mediterranean coast and Ebro basin. The data assimilation improves those results, obtaining comparable values to those from ERAI (mean r for D was 0.48 and 0.51 for ERAI). However, both ERAI and the D experiment showed their poorest results for the Mediterranean coast and the north-western IP. Similar spatial pattern and results were obtained if comparing to GLEAM v3.0c dataset, with 0.33, 0.47 and 0.51 as mean values of r for N, D and ERAI respectively (not shown).

Results for the evaporation bias are presented in Figure 27. For the N experiment, the best results were observed inland. Some major differences appeared near the southern and south-eastern coasts of the IP, but the mean bias was only -0.01 mm/day for this experiment.

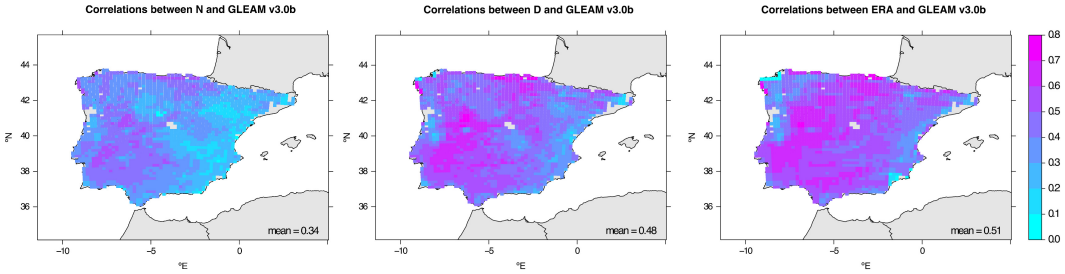

Figure 8. Evaporation correlation maps between GLEAM (version 3.0b) for both WRF simulations and ERAI. All of the problematic points presented in Figure 25 are eliminated from this validation. The mean r values are presented in the right bottom corner of the maps.

Both the D experiment and ERAI showed a negative bias, being more remarkable for ERAI (-0.26 mm/day and -0.82 mm/day respectively). No clear pattern was observed for the D experiment, but differences near the coasts were remarkable for ERAI. Similar results were obtained with GLEAM v3.0c, with -0.05 mm/day, -0.32 mm/day and -0.86 mm/day biases for N, D and ERAI respectively (not shown).

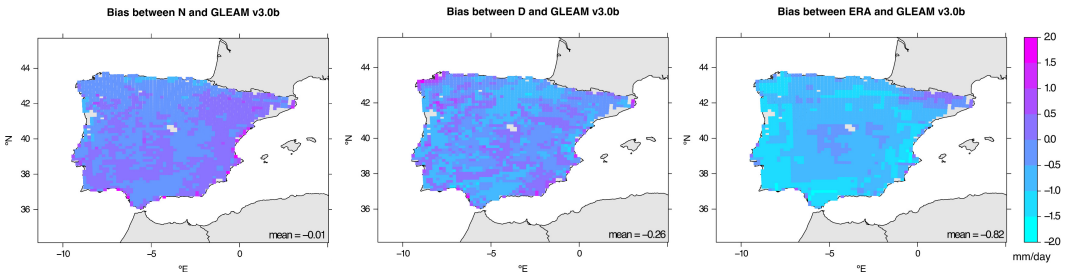

Figure 9. Same as Figure 26 but for bias (mm/day).

The effect of removing all urban points in the validation was observed particularly in the r and bias measured for both WRF experiments. A quantile analysis of the values before and after removing these problematic points can help us to quantify its effect. Focusing on the GLEAM v3.0b dataset and the N experiment, the 97.5, 50 and 2.5 percentiles for r vary from 0.51, 0.34 and 0.09 to 0.51, 0.35 and 0.17 respectively if the urban points are not included. For the D experiment, the values of the percentiles changed from 0.66, 0.48 and 0.06 to 0.66, 0.48 and 0.27 respectively. Focusing on the bias between GLEAM v3.0b and the N experiment, the highest percentiles are reduced from 1.23, 0 and -0.48 to 0.5, -0.01 and -0.48. For the D experiment, they vary from 1.27, -0.31 and -0.9 to 0.52, -0.34 and -0.9 respectively. Same features are observed for the r and biases between GLEAM v3.0c and both WRF simulations. Therefore, the results are quite robust in the central part of the probability distribution function of the verification scores.

The areal mean of the monthly evaporation (Figure 28) showed a similar spatially averaged evaporation rate for GLEAM and both WRF experiments. An intensified behaviour was observed for ERAI over the IP. The bias between ERAI and GLEAM v3.0b varied from 0.59 mm/day in winter to 1.11 mm/day in summer. For GLEAM v3.0c, a bias of 0.6 mm/day in winter and 1.30 mm/day in summer were measured.

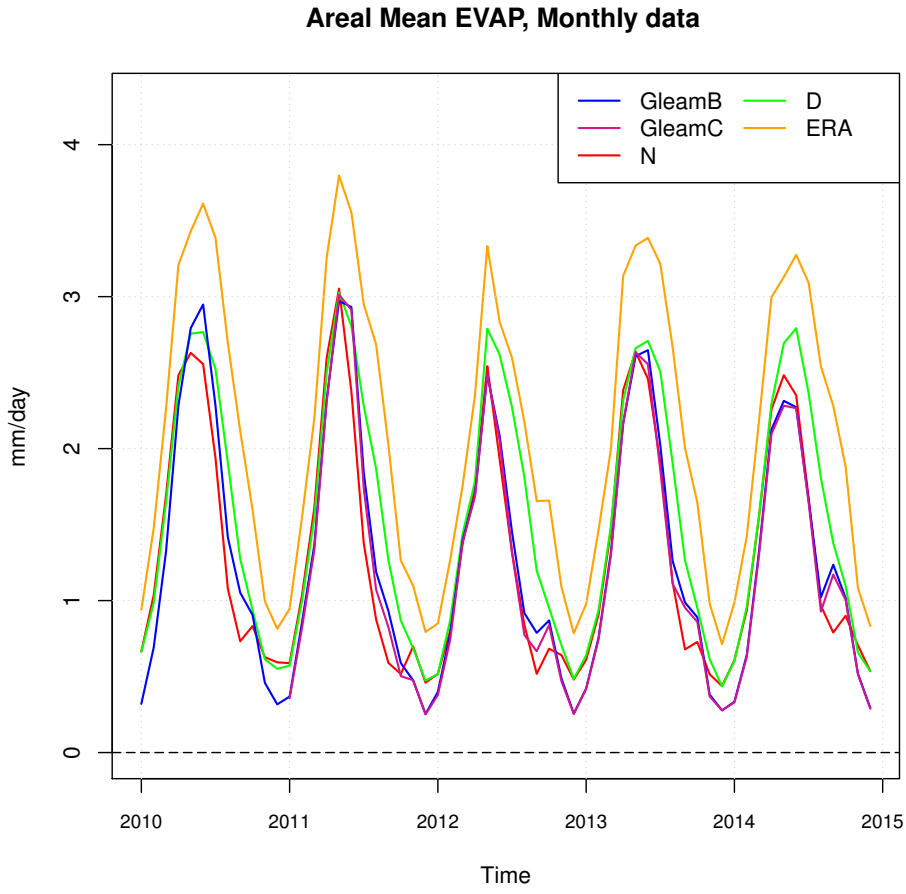

Figure 10. Areal mean evaporation simulated by different datasets and experiments for 2010-2014. GLEAM v3.0b in blue, GLEAM v3.0c in magenta, the N experiment in red, the D experiment in green and ERAI in orange.

3.4 Analysis of the residual and analysis increments

The most important terms of equation 1 were determined analysing the spread of their areal mean values. This analysis showed that terms relative to condensates can be disregarded, as previously found by other studies [*Peixoto and Oort*, 1992; *Snider*, 2000]. Figure 29 shows the distribution of the areal mean monthly data, that is, the main terms of the water balance according to equation 1. Thus, the leading terms of the water balance were the tendency of the IWV, the divergence of moisture flux, evaporation and precipitation. ERAI produced a larger residual than both WRF experiments. Both the D and N experiments showed a similar residual but with opposite signs. The change in sign from the N to the D experiment can be unequivocally attributed to the 3DVAR assimilation step since both experiments are configured the same way. Additionally, the D experiment showed a better agreement with observations during the verification. It has also proved to be the one with better (or at least, similar) results than ERAI for each term of the water balance. Taking this feature into account, a deeper analysis of the residual and the water balance of the experiment D was carried out.

Figure 30 shows the distribution of the areal mean values of the residual according to the hour and season for the D experiment. The spread of the residual was bigger during

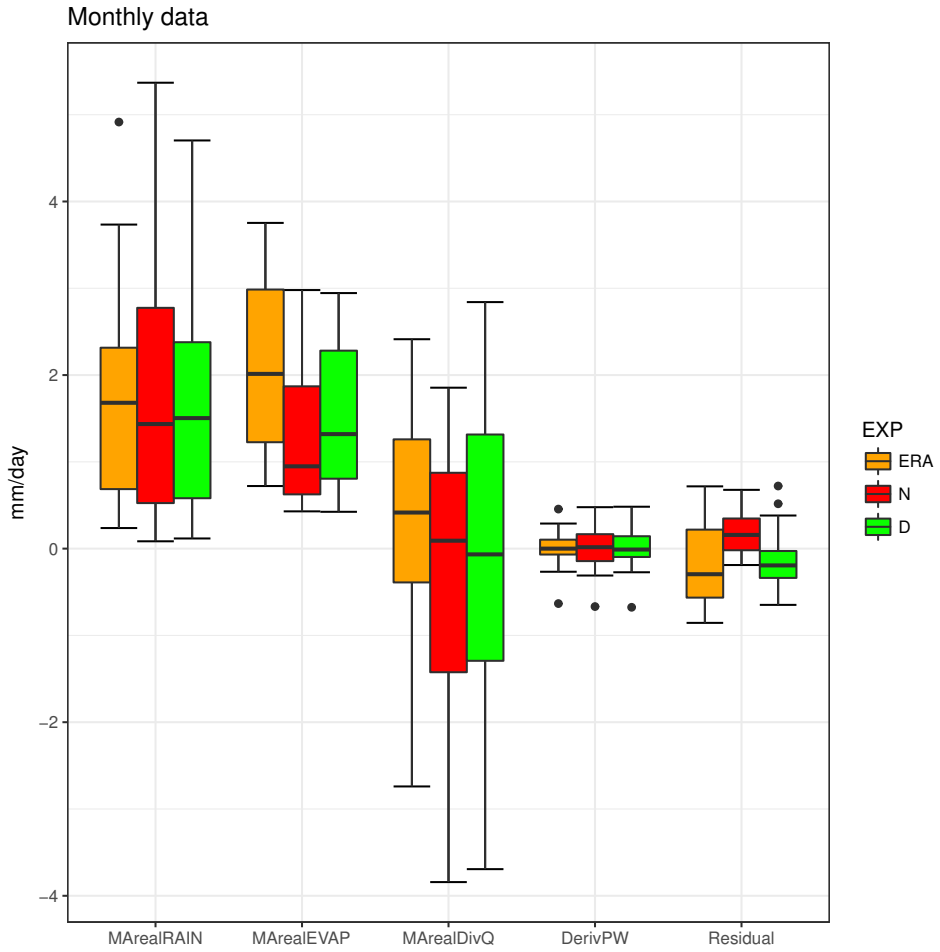

Figure 11. Areal mean of the precipitation (MArealRAIN), the evaporation (MArealEVAP), the divergence of moisture flux (MArealDivQ), the tendency of the IWV (DerivQ) and the residual according to the experiment: ERAI in orange, the N experiment in red and the D experiment in green (mm/day).

summer (JJA), and smaller during winter (DJF). A similar distribution was observed during spring (MAM) and autumn (SON). The largest residuals appeared at 18 UTC.

In order to analyse the role played by analysis increments in the structure of the residual, Figure 31 shows the distribution of the analysis increment of the specific humidity at 2m during the data assimilation process at different times and seasons. Large analysis increments in moisture at 12 UTC and 18 UTC for each season were observed. The spatial pattern at 12 UTC was more intense than that at 18 UTC, but both showed great values in the Ebro and Guadalquivir basins, south of Madrid and southeastern IP. Differences between seasons were highlighted, with strong increments in summer, but less during winter. However, the spatial pattern was more or less constant in every season (not shown).

In order to finish with the study of the moisture balance terms with the structure of the residual, an analysis by means of principal components of the area averaged terms $\left[\frac{\partial W}{\partial t}\right]$, $\left[\vec{\nabla}\cdot\vec{Q}\right]$, $[E]$ and $[P]$ shows that the leading principal components explain 72% of the total variance with anomalies of the same sign tied to $\left[\frac{\partial W}{\partial t}\right]$ and (weaker) $[P]$. In this leading PC, an opposite sign in the anomalies corresponds to $\left[\vec{\nabla}\cdot\vec{Q}\right]$. The second principal component explains 20% of the total variance, and it basically represents the variability of $[P]$ with a

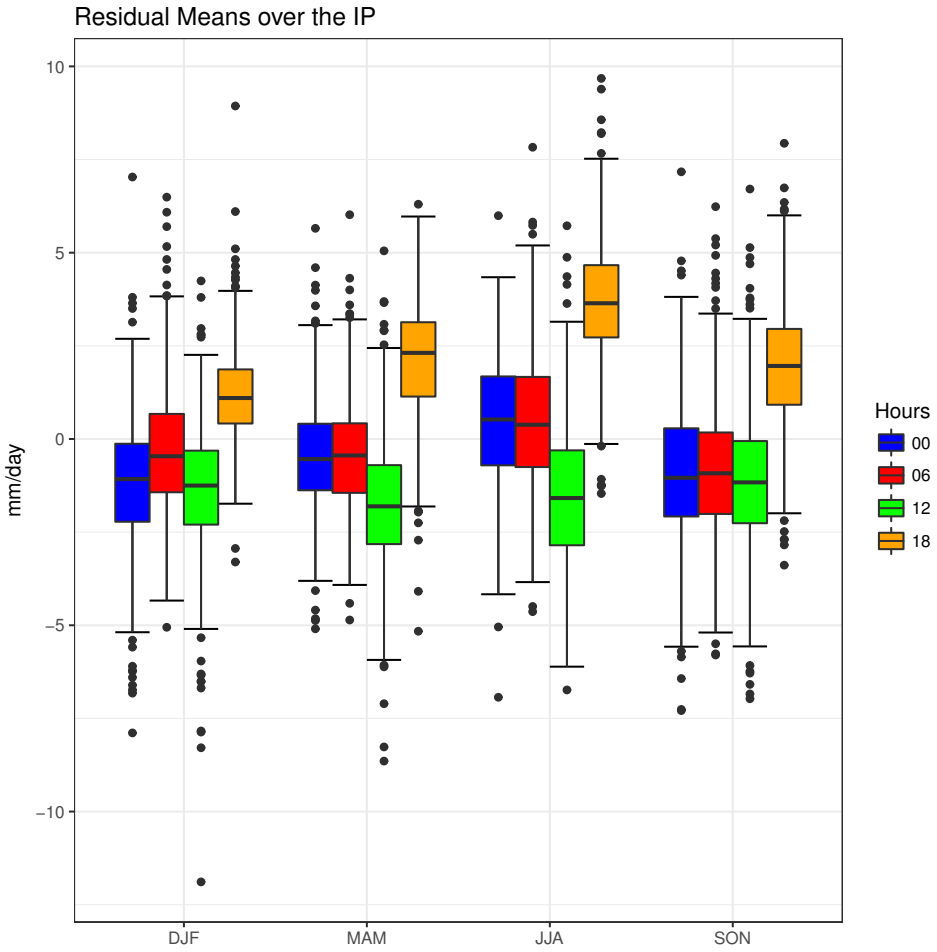

Figure 12. Areal mean of the residual over the IP according to the D experiment stratified by season (winter DJF, spring MAM, summer JJA, autumn SON) and hour (00 UTC, 06 UTC, 12 UTC and 18 UTC in blue, red, green and orange respectively).

much weaker contribution (with opposite sign) of $[E]$ and $\left[\frac{\partial W}{\partial t}\right]$. Finally, the third PC represents only 6% of the total variance. It projects almost exclusively onto $[E]$, and its time series shows a clear seasonal pattern with higher values during summer. It explains 77% of the variability of $[E]$. However, since neither of these PCs nor the original variables are strongly linearly related with the residual, there is no simple explanation for its area-averaged values.

Regarding the analysis minus background of the temperature at 2m, the most remarkable increments were observed at 00 and 12 UTC of every season (not shown). Increments occurred particularly in the south of the IP during winter, and they reached the Cantabrian Range in summer. The assimilation substantially corrects (map not shown) the well known cold bias in summer temperatures observed in this region for WRF simulations [*Fernández et al.*, 2007; *Argüeso et al.*, 2011; *Jerez et al.*, 2012]. However, an analysis of the physical mechanisms in this case are left for further research, since the topic of this paper is not focusing on that.

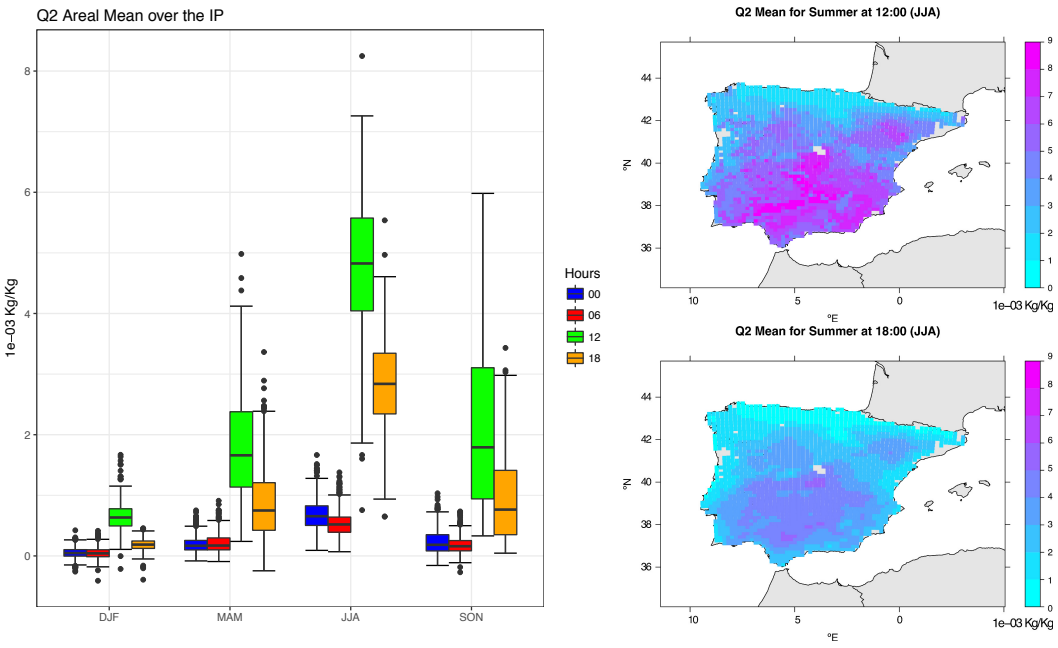

Figure 13. Left: Areal mean over the IP of the analysis minus background of the specific humidity at 2m (1×10^{-3} kg/kg) according to the season (winter DJF, spring MAM, summer JJA, autumn SON) and hour (00, 06, 12 and 18 UTC in blue, red, green and orange respectively). Right: Spatial distribution of the analysis minus background during summer at 12 UTC (top) and 18 UTC (bottom).

3.5 Description of the main features of the hydrological cycle

After having shown that the D experiment accurately simulates the structure of the hydrological cycle over the IP, this subsection describes the main features of this cycle. First, the accumulated annual values of evaporation for the D experiment did not show a clear pattern over the IP. However, if we check the mean daily values of evaporation for winter and summer (Figure 32), some features can be observed. During winter, the evaporation of the IP is really small (0.67 mm/day on average), and the largest values are located in the south of Portugal. During summer, remarkable values (above 4 mm/day) are observed in the north and north-western IP, the areas where the soil has the highest moisture content during summer. Spring and autumn are intermediate seasons regarding this variable but show no special structure (maps not shown).

For precipitation, however, the influence of the Atlantic sources of moisture was recognizable (Figure 33). The D experiment obtained a similar pattern to that obtained by AEMET for 1971-2000. This pattern was not so clear for the EOBS dataset. A good agreement between the D experiment and ECA&D dataset was observed. Only in a few stations of the southwestern IP can be observed an underestimation on the precipitation amount simulated by the D experiment, probably related to the difficulties simulating the convective precipitation regimes that dominate this region.

Seasonal analysis of the IWV showed higher values in the Mediterranean coast and the Ebro basin during summer (Figure 34). Remarkable values were also observed near the Bay of Biscay. During the other seasons, especially spring and autumn, the IWV values were higher in the most important basins of the IP: Guadalquivir, Guadiana, Tagus and Ebro basins. The smallest values were located near the mountain ranges during winter, as could be expected from the lower temperatures at low levels of the atmosphere and the smaller height of the troposphere at those places.

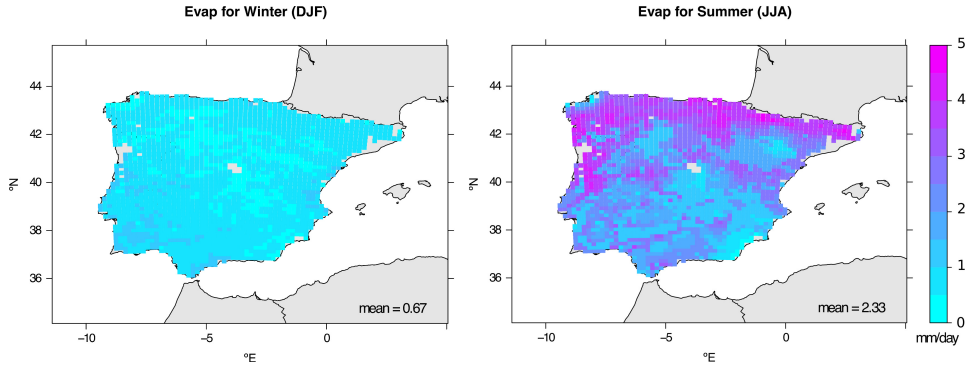

Figure 14. Mean daily evaporation (mm/day) simulated by the D experiment over the IP for winter (left) and summer (right). The mean value of the evaporation over the IP is presented in the right bottom corner of the maps.

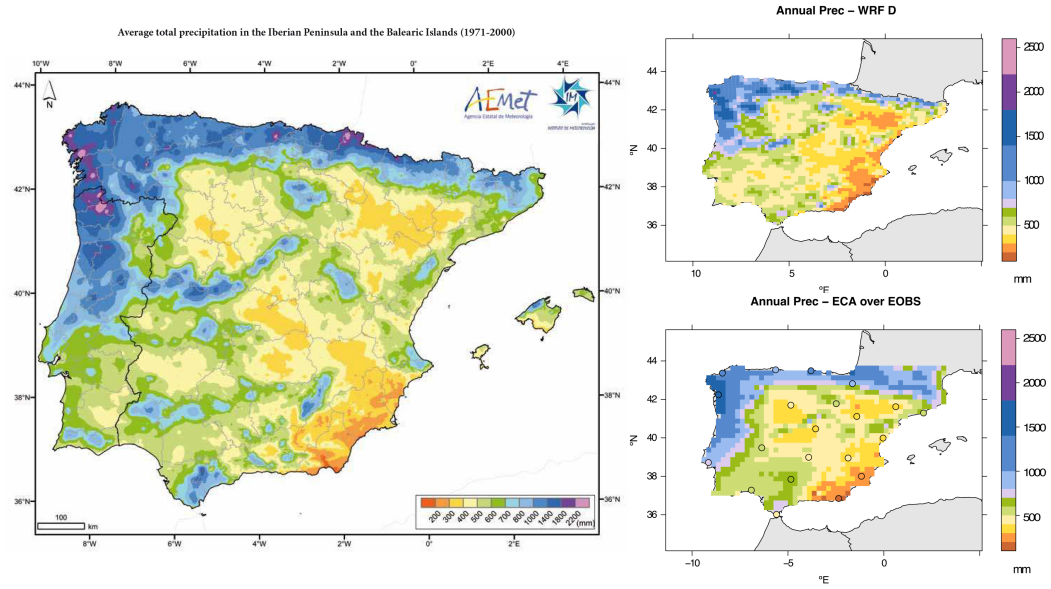

Figure 15. Accumulated annual precipitation (mm) over the IP taken from the Spanish Meteorological Agency atlas [*AEMET*, 2011] for 1971-2000 (left), compared to those from the D experiment (top right) and from ECA&D over EOBS (bottom right).

An advantage of using a mesoscale model is that it allows to represent new fields that can not be properly estimated from observations alone. This is the case of the moisture that crosses the boundaries of the IP. Figure 35 shows the transboundary moisture fluxes across the boundaries of the IP during winter as simulated by the D WRF experiment. In this case, these results were not compared to the transboundary fluxes from ERAI. According to the net values of each studied hour (00 UTC, 06 UTC, 12 UTC and 18 UTC), the IP imports a great amount of moisture during this season. The overall net flux is always negative, in the range of $[-35, -13]$ Pg/mon, with less import during night. The moisture enters the IP mainly through the Portuguese coast and exits the peninsula through the Mediterranean coast. During Spring (not shown), the IP exports moisture at night (30 Pg/month), but imports it during the day (-27 Pg/mon).

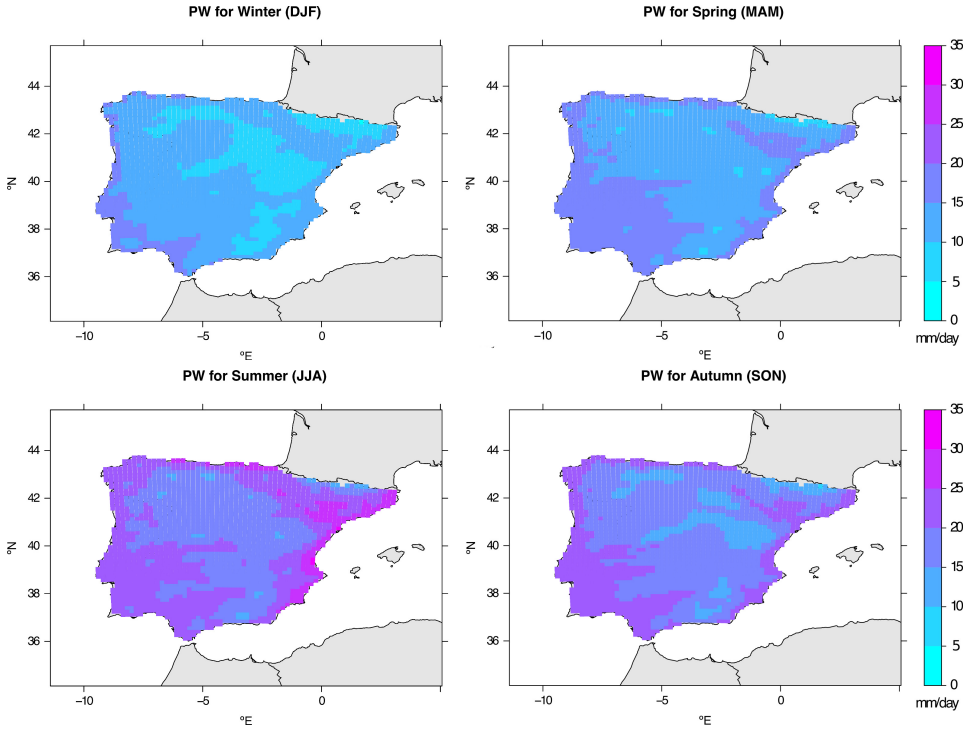

Figure 16. Mean daily IWV (mm) simulated by the D experiment over the IP for winter (top left), spring (top right), summer (bottom left) and autumn (bottom right).

During summer (Figure 36), the IP exports moisture during the whole day (net flux always positive ranging from 48 to 68 Pg/mon) except at 12 UTC and 15 UTC that the IP moisture flux is negative (-0.34 and -8 Pg/mon respectively). At those times, moisture is imported specially because of the breezes in the Alboran Sea (southern Spain) (see Figure 36, 06 UTC versus 18 UTC). This breeze reaches its maximum intensity slightly later than 12 UTC. During Autumn (not shown), the IP mainly imports moisture (net flux ranges from -31 Pg/mon to 4 Pg/mon).

4 Discussion

In this section, we begin by restating the main objectives of this paper: to carry out an analysis of the whole atmospheric branch of the water cycle over the Iberian Peninsula and to analyse the benefits of applying a 3DVAR data assimilation step while running WRF when studying the atmospheric moisture balance. To do so, two simulations covering a five-year-period were created. The five year period is as long as those typically used in the field when analyzing the performance of different configurations of WRF in many applications such as *Jiménez and Dudhia* [2013], *Rios-Entenza and Miguez-Macho* [2014], *Rios-Entenza et al.* [2014] and *Ulazia et al.* [2016]. The use of five years makes it clear that our WRF simulations cannot be used in a full study of the long-term climatology of the elements of the water balance and their interannual variability. However, it has been checked if our results are related to low frequency variability sources such as the NAO, a well known factor affecting the variability of precipitation over the area [*Rodríguez-Puebla et al.*, 2001]. Additional checks were performed with El Niño-Southern Oscillation (ENSO), even if previous analyses stated that its effects are restricted to different sectors of the IP [*Kiladis and Diaz*, 1989; *Rodó et al.*, 1997; *Frías et al.*, 2010; *Vicente-Serrano et al.*, 2011; *Lorenzo et al.*, 2011] and that the effect by the ENSO is not stationary [*López-Parages and Rodríguez-Fonseca*, 2012]. After

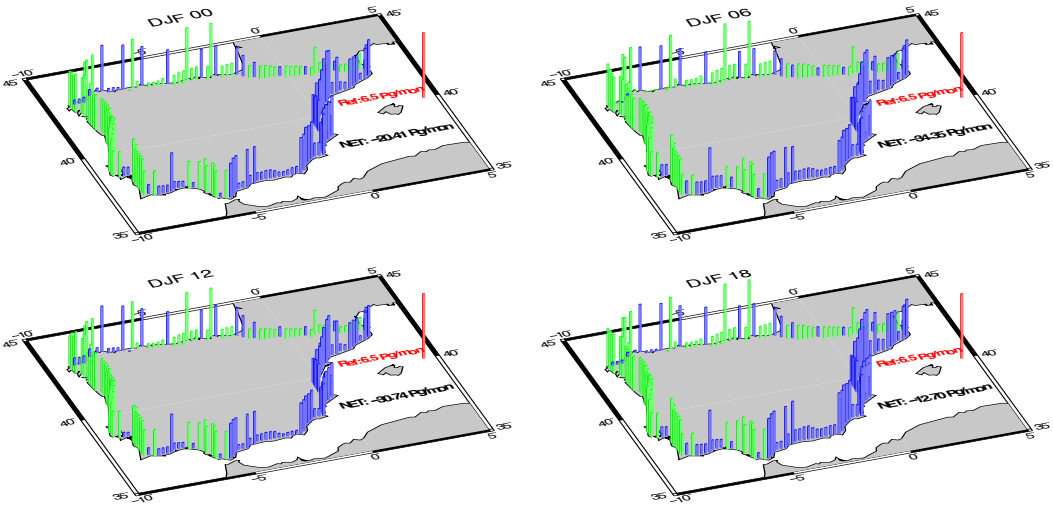

Figure 17. Transboundary moisture fluxes analysis at 00 UTC (top left), 06 UTC (top right), 12 UTC (bottom left) and 18 UTC (bottom right) during winter. The reference bar is labelled at 6.5 Pg/month. The green bars represent an inland flux, while the blue bars refer to an outward flux.

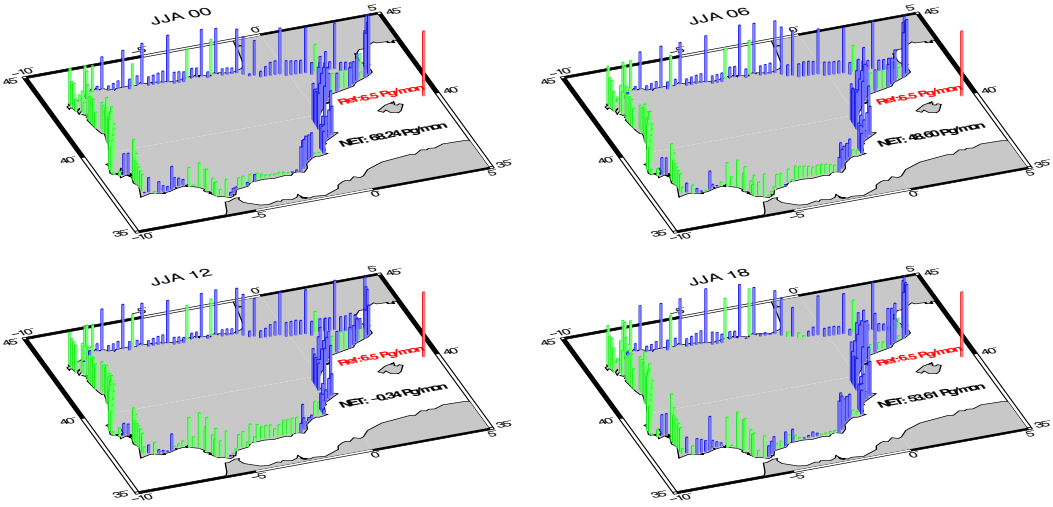

Figure 18. Same as Figure 35 but for summer.

classifying every month into high (above the 75th percentile) or low (below the 25th percentile) values of NAO and ENSO index (downloaded from the Climate Prediction Center), the residuals of the moisture equation where compared. This comparison shows that they do not change with the different phases during our five-year period (results not shown).

Both WRF simulations include a one-year spin-up as we are not trying to initialize every layer of the land surface model during that period. Several years are needed to achieve this goal in land-moisture data assimilation systems [*Lim et al.*, 2012; *Stacke and Hagemann*, 2016]. However, our intention is to get low errors in the fluxes between the land and the atmosphere, as we will focus only in the atmospheric branch of the water cycle, not in moisture deep soil layers. According to recent studies [*Montavez et al.*, 2017], the optimal initialization is obtained for a 6-month spin-up over the EUROCORDEX domain. However, *Giorgi and Bi* [2000] stated that the RMSD reaches the equilibrium after 5-15 days of simulation

and *Christensen* [1999] suggested that a few months spin-up prevents errors in the soil variables related to a poor initialization. Different periods have been used for spin-up of the soil model in previous studies, such as one month [*Angevine et al.*, 2014], four months [*Jerez et al.*, 2010, 2012, 2013], seven months [*Argüeso et al.*, 2011] or one year [*Zheng et al.*, 2017]. In any case, the D experiment we present is not a climatic simulation, so any problem in the run (if any) would be corrected by the 3DVAR data assimilation step. In addition, the effect of selecting a longer spin-up period on the residuals was studied (not shown). Even if the spin-up period was increased to 5 years using for validation shorter periods in our integration, the spread of the residuals of both WRF experiments with respect to the ones from ERAI were not affected by that change.

Considering the differences in the spread of the residual between both N and D WRF experiments, the results showed that the experiment without data assimilation (N) produced a positive residual of the water balance whilst, conversely, the D experiment with data assimilation every six hours produced in general a negative residual. This change is due to the analysis increments in the D experiment. The objective of the data assimilation process during the WRF simulations is to create accurate initial fields, closer to the state of the atmosphere measured by the observations, thus correcting biases that exist in the model. This is particularly relevant for balance equations, such as the moisture conservation equation, as the analysis procedure cannot preserve moisture (by definition) since analysis increments are not physical terms of the atmosphere. However, the analysis performed shows that analyses resulting from the D experiment are closer to observations than output fields from the N experiment. Despite the lack of complete balance, these analyses represent better the hydrological cycle than the simulation in the N experiment and than the coarse fields from the forcing reanalysis ERA Interim. Our results show consistently that 3DVAR data assimilation improves the quality of the simulated variables as also found by *Navascués et al.* [2013] and *Ulazia et al.* [2016]. Thus, the use of 3DVAR data assimilation improves the balance according to this bootstrap-based robust evaluation.

The robustness of our results was also checked by means of a bootstrap analysis of the residuals. 1000 random time series were sampled from both WRF experiments and ERAI, and the distribution of their medians showed that the seasonal cycle is more intense that the interannual variability over the IP (not shown). Additionally, the Median Absolute Deviation (MAD) between these new and the original time series is really small for the N and D experiments compared to ERAI's. The spread of the values do not overlap each other (not shown). According to our group's previous results [*Ulazia et al.*, 2016], this is also the case for wind over the ocean for a ten year period when comparing WRF runs with (every six and twelve hours) or without data assimilation.

The lack of fine resolution datasets for validation (particularly for our period and/or domain) is a problem for the interpretation of the results. It is clear that the relatively coarse resolution of some observational datasets produces a mismatch in the initial interpretation of the results. This is what happens particularly with the EOBS dataset. According to the validation results for precipitation (Figures 23 and 24), the bias showed major discrepancies between EOBS dataset and both WRF experiments near the mountain regions of the IP. However, if we take into account the accumulated annual precipitation amount (Figure 33, right), the pattern observed for the D experiment is much closer to the observations than that for EOBS. This means that if finer resolution datasets existed, the verification results for both WRF integrations might be better, since the produced fields show a geographical distribution that is closer to the one available from high resolution fields corresponding to a different period. This is also extensible to the other precipitation datasets used for validation, as all of them have similar resolutions. In addition, the most similar dataset available to our experiments would be the Iberian dataset (0.2° resolution) [*Belo-Pereira et al.*, 2011], created by merging the Spain02 dataset [*Herrera et al.*, 2012, 2016] with the PT02 dataset (for Portugal). However, its period (1950-2003) does not cover ours, so that it cannot be directly used, although it can be qualitatively compared. Even if the results for precipitation correspond

to different periods of time, the accumulated annual precipitation over the IP for the Iberian dataset showed a similar pattern (see Figure 6 from *Belo-Pereira et al.* [2011]) to that observed in both WRF experiments and the one taken from the atlas created by the Spanish Meteorological Agency [*AEMET*, 2011]. This strengthens the idea that not having access to high-resolution and real datasets is a problem for performing a proper validation of these new high resolution simulations.

Comparing gridded datasets with point measurements can be also problematic, as the open problem of the representativeness error is introduced. According to *Tustison et al.* [2001], the representative error is a non-zero scale-dependant error and it is independent of the model performance. Usually, there are two ways to compare different datasets: using the nearest neighbour or the bilinear interpolation. The first technique is used when dealing with non-linear fields [*Casati et al.*, 2008; *Moseley*, 2011] as it does not smooth the field when downscaling to higher resolution grid [*Accadia et al.*, 2003]. On the other hand, the bilinear interpolation is suitable for grids that not vary too much on scales longer than the spatial resolution [*Moseley*, 2011], but it reduces the maxima and increases the minima of precipitation data [*Accadia et al.*, 2003]. This information supports the idea that the nearest neighbour technique is the best for our study. In addition, it has customarily been used in previous studies [*Borge et al.*, 2008; *Jiménez et al.*, 2010; *Jiménez and Dudhia*, 2012; *Önol*, 2012; *Soares et al.*, 2012]. Previous studies also identified that the verification of limited-area high resolution model output is problematic due to the difficulty in having access to observational data with the needed time and spatial resolutions [*Rummukainen*, 2010; *Gómez-Navarro et al.*, 2012].

The poor r values obtained for precipitation in the Mediterranean region (Figure 5) are related to its generally convective origin. The Atlantic facade is mainly affected by frontal systems, while the Mediterranean coast and the Ebro Valley are characterized by very scarce precipitation concentrated in high precipitation events. This convective precipitation is difficult to be detected even by the observational datasets [*Herrera et al.*, 2012], and the different spatial structure of these precipitation types has been extensively studied [*Fernández et al.*, 2003; *Muñoz-Diaz and Rodrigo*, 2004; *Rodríguez-Puebla et al.*, 1998; *Esteban-Parra et al.*, 1998b; *García-Valdecasas Ojeda et al.*, 2017]. Therefore, many models perform better over the Atlantic area than over the Mediterranean region [*Domínguez et al.*, 2013; *Jiménez-Guerrero et al.*, 2013]. Regarding the r for the evaporation (Figure 8), the poor values are located in the same region in both WRF experiments, but also in ERAI. To the best of authors' knowledge, there has not been any other validation of the GLEAM dataset over the IP, and as the measurements of evaporation are not common, the reason why this values are concentrated in that region is an interesting open question for future work. That is, in any case, limited by the availability of evapotranspiration observations.

The time series of evaporation in some points were flat most of the times, highlighting WRF's inability to simulate the seasonal variability, and the r of evaporation with observations at those isolated points were rather low. The analysis of the static data for the land surface model showed that the WRF model was not able to simulate a realistic evaporation in those grid points because the land use was configured as urban or built-up. Land surface model's soil types across the IP were analysed, and the domain is mainly made of loam, with the exception of the Guadalquivir Basin that is made of clay. As similar soil types were located across the entire IP, the urban or built-up category seemed to be the cause of this problem, since the points affected by this were all of the same type.

The seasonal and hourly analysis of the areal mean of the residuals (Figure 30) have shown that the most remarkable values appeared at 18 UTC, and this must be related to the impact of the assimilation of observations (temperature and/or moisture) in the planetary boundary layer (PBL).

The effect of the breeze near the coasts of the IP was highlighted in our results. The analysis increments for the specific humidity at 2m (Figure 31) showed that important changes

take place during the afternoon, and they seem to be related to the coastal breezes in the Mediterranean coast. The effect of those breezes is also remarkable in the Ebro and Guadalquivir basins, which is similar to the results obtained by *Cardoso et al.* [2013], as they found that the inland moisture enters the IP through the basins. The relevance of the breeze was also shown by *Ortiz de Galisteo et al.* [2011] for the annual and seasonal diurnal cycles of IWV on the basis of the analysis of GPS data. In addition, the high values of IWV detected in summer in the Mediterranean and Cantabrian coasts seemed to be related to the breezes in those regions. This feature resembles *Zveryaev et al.* [2008], as they found that summer heating and local convective processes can cause positive IWV anomalies even if the moist transport diminishes. Our results regarding IWV fields resemble findings by *Zveryaev et al.* [2008] that showed large values of IWV over coastal regions in winter and largest values near the Mediterranean in summer.

5 Conclusions and future outlook

We analysed the differences in the water balance simulated by two WRF simulations: one of them (D) included 3DVAR data assimilation four times a day and a second one (N) did not. The spatial resolution of these runs (15 km x 15 km) makes them interesting for the study of the atmospheric water balance. Then, this comparison allowed us to evaluate the advantages and disadvantages of using the data assimilation and to check the closure of the balance over the complex landscapes and climatic areas of the IP. ERAI reanalysis data and several datasets were used for the validation of each term of the water balance equation.

Each element of the water balance was independently validated. IWV results showed that the D experiment remarkably improved the r, standard deviation and RMSE values of the N experiment for eight radiosondes located all over the IP. It also improved the results of ERAI. Compared to data measured by MODIS, the D experiment improved the r obtained by the N experiment in the southern and south-western IP, and even reached comparable values to those obtained by ERAI.

The validation of precipitation with EOBS showed that ERAI and both WRF experiments exhibited poor r values near the Mediterranean coast and Ebro basin. The N experiment yielded the poorest results, but the D experiment outperformed ERAI in the south of IP. Compared to ECA&D, TRMM or GPCP datasets, the D experiment was able to obtain comparable results to those from ERAI.

Regarding the evaporation, every urban or built-up grid point were eliminated from the validation, since WRF was not able to simulate a realistic evaporation in those grid points. Then, compared to GLEAM v3.0b and v3.0c datasets, comparable results were observed for the D experiment and ERAI. However, poor r values were obtained in both experiments in the Mediterranean coast and the north-western IP. The evaporation rate simulated by both GLEAM datasets and both WRF simulations over the whole area were similar. For ERAI, its evaporation rate overestimates the rate by other datasets.

The analysis of the residual (equation 2) showed the leading terms of the water balance to be the tendency of the IWV, the divergence of moisture flux, evaporation and precipitation, with condensates playing a minor role as usual in this kind of studies [*Hirschi et al.*, 2006]. The effects of the 3DVAR data assimilation were perceptible in the changes of the residual within a day, particularly at 18 UTC. Those changes were very likely related with the assimilation of temperature and moisture observations in the lower levels (Figure 31). No distinctive spatial patterns were detected for the residual and for the evaporation. However, the influence of the Atlantic fronts was highly recognizable in the annual accumulated precipitation maps. High values of IWV were observed in the coastal zones of Spain during summer.

The transboundary moisture fluxes showed differences in the behaviour of the IP depending on the season. In winter, the IP imports a great amount of moisture during the whole

day. During spring, summer and, to a lesser extent, autumn, the IP mainly exports moisture through the Mediterranean coast, a result similar to continental US [*Berbery and Rasmusson*, 1999]. Only during midday, moisture is imported due to the sea breeze, particularly in the south of Spain.

In summary, our results showed that the D experiment improved the results obtained by the N experiment, that is, the runs using 3DVAR data assimilation every 6 hours (at 00 UTC, 06 UTC, 12 UTC and 18 UTC) improved the quality of results obtained using the high-resolution model alone (traditional numerical downscaling). Furthermore, some of the products shown indicated that the numerical output has some verification scores that outperform the driving reanalysis in the case of IWV, precipitation or evaporation, thus adding value to the forcing reanalysis.

Finally, there are still open questions in this area such as the identification of the physical mechanisms that explain WRF's inability to simulate a realistic evaporation in urban grid points, the effect of improving the spatial and/or temporal resolution of the boundary conditions in both WRF simulations, or the energy fluxes involved in the summer cold bias in temperature in the south of the IP.

Acknowledgments

This work was supported by grants (CGL2013-45198-C2-1-R and CGL2016-76561-R, MINECO / ERDF, UE). SJGR is supported by a FPI Predoctoral Research Grant (MINECO, BES-2014-069977). Additional funding was received from the University of the Basque Country (UPV/EHU, GIU 14/03). Intensive computational resources used in the project were provided by I2BASQUE. The authors thank the creators of the WRF/ARW and WRFDA systems for making them freely available to the community. The authors acknowledge the E-OBS dataset from the EU-FP6 project ENSEMBLES and the data providers in the ECA&D project. Some maps where plotted using Generic Mapping Tools (GMT), and many of the calculations were carried out using the R programming language (version 3.2.4). The authors acknowledge the creators of many R-packages: reshape2, RNetCDF, ggplot2, plotrix, sp, maptools, rgdal, maps, mapdata, shape, lubridate, kza, grid, xtable and RColorBrewer. The data used to produce this paper is publicly available (ERA Interim, ECA&D, GLEAM, EOBS, and so on). Authors thank two anonymous reviewers for their insightful comments that have led to an improved version of the paper. The data produced by the model needed to reproduce these results are publicly available and it can be download from `http://www.ehu.eus/eolo/data.html` or from the CERA/DKRZ archive at `http://cera-www.dkrz.de/WDCC/ui/Compact.jsp?acronym=WaVaCurIP`.

References

Accadia, C., S. Mariani, M. Casaioli, A. Lavagnini, and A. Speranza (2003), Sensitivity of precipitation forecast skill scores to bilinear interpolation and a simple nearest-neighbor average method on high-resolution verification grids, *Weather and Forecasting*, *18*(5), 918–932, doi:10.1175/1520-0434(2003)018<0918:SOPFSS>2.0.CO;2.

AEMET (2011), *Atlas climático ibérico: Temperatura del aire y precipitación (1971-2000)*, Agencia Estatal de Meteorología (AEMET).

Angevine, W. M., E. Bazile, D. Legain, and D. Pino (2014), Land surface spinup for episodic modeling, *Atmospheric Chemistry and Physics*, *14*(15), 8165–8172, doi: 10.5194/acp-14-8165-2014.

Argüeso, D., J. M. Hidalgo-Muñoz, S. R. Gámiz-Fortis, M. J. Esteban-Parra, J. Dudhia, and Y. Castro-Díez (2011), Evaluation of WRF parameterizations for climate studies over southern Spain using a multistep regionalization, *Journal of Climate*, *24*(21), 5633–5651, doi:10.1175/JCLI-D-11-00073.1.

Barker, D., X.-Y. Huang, Z. Liu, T. Auligné, X. Zhang, S. Rugg, R. Ajjaji, A. Bourgeois, J. Bray, Y. Chen, M. Demirtas, Y.-R. Guo, T. Henderson, W. Huang, H.-C. Lin, J. Micha-

lakes, S. Rizvi, and X. Zhang (2012), The Weather Research and Forecasting model's community variational/ensemble data assimilation system: WRFDA, *Bulletin of the American Meteorological Society*, *93*(6), 831–843, doi:10.1175/BAMS-D-11-00167.1.

Belo-Pereira, M., E. Dutra, and P. Viterbo (2011), Evaluation of global precipitation data sets over the Iberian Peninsula, *Journal of Geophysical Research: Atmospheres*, *116*(D20), doi:10.1029/2010JD015481.

Berbery, E. H., and E. M. Rasmusson (1999), Mississippi moisture budgets on regional scales, *Monthly Weather Review*, *127*(11), 2654–2673, doi:10.1175/1520-0493(1999)127<2654:MMBORS>2.0.CO;2.

Borge, R., V. Alexandrov, J. J. del Vas, J. Lumbreras, and E. Rodríguez (2008), A comprehensive sensitivity analysis of the WRF model for air quality applications over the Iberian Peninsula, *Atmospheric Environment*, *42*, 8560–8574, doi:10.1016/j.atmosenv.2008.08.032.

Cardoso, R. M., P. M. M. Soares, P. M. A. Miranda, and M. Belo-Pereira (2013), WRF high resolution simulation of Iberian mean and extreme precipitation climate, *International Journal of Climatology*, *33*(11), 2591–2608, doi:10.1002/joc.3616.

Casati, B., L. J. Wilson, D. B. Stephenson, P. Nurmi, A. Ghelli, M. Pocernich, U. Damrath, E. E. Ebert, B. G. Brown, and S. Mason (2008), Forecast verification: Current status and future directions, *Meteorological Applications*, *15*(1), 3–18, doi:10.1002/met.52.

Christensen, O. B. (1999), Relaxation of soil variables in a regional climate model, *Tellus A*, *51*(5), 674–685, doi:10.1034/j.1600-0870.1999.00010.x.

Dee, D. P., S. M. Uppala, A. J. Simmons, P. Berrisford, P. Poli, S. Kobayashi, U. Andrae, M. A. Balmaseda, G. Balsamo, P. Bauer, P. Bechtold, A. C. M. Beljaars, L. van de Berg, J. Bidlot, N. Bormann, C. Delsol, R. Dragani, M. Fuentes, A. J. Geer, L. Haimberger, S. B. Healy, H. Hersbach, E. V. Hólm, L. Isaksen, P. Kållberg, M. Köhler, M. Matricardi, A. P. McNally, B. M. Monge-Sanz, J.-J. Morcrette, B.-K. Park, C. Peubey, P. de Rosnay, C. Tavolato, J.-N. Thépaut, and F. Vitart (2011), The ERA-Interim reanalysis: Configuration and performance of the data assimilation system, *Quarterly Journal of the Royal Meteorological Society*, *137*(656), 553–597, doi:10.1002/qj.828.

Domínguez, M., R. Romera, S. E, L. Fita, J. Fernández, P. Jiménez-Guerrero, J. P. Montávez, W. D. Cabos, G. Liguori, and M. A. Gaertner (2013), Present-climate precipitation and temperature extremes over Spain from a set of high resolution RCMs, *Clim. Res.*, *58*, 149–164, doi:10.3354/cr01186.

Dosio, A. (2016), Projections of climate change indices of temperature and precipitation from an ensemble of bias-adjusted high-resolution EURO-CORDEX regional climate models, *Journal of Geophysical Research: Atmospheres*, *121*, 5488–5511, doi:10.1002/2015JD024411.

Eiras-Barca, J., S. Brands, and G. Miguez-Macho (2016), Seasonal variations in North Atlantic atmospheric river activity and associations with anomalous precipitation over the Iberian Atlantic margin, *Journal of Geophysical Research: Atmospheres*, *121*, 931–948, doi:10.1002/2015JD023379.

Esteban-Parra, M. J., F. S. Rodrigo, and Y. Castro-Diez (1998a), Spatial and temporal patterns of precipitation in Spain for the period 1880-1992, *International Journal of Climatology*, *18*(14), 1557–1574, doi:10.1002/(SICI)1097-0088(19981130)18:14<1557::AID-JOC328>3.0.CO;2-J.

Esteban-Parra, M. J., F. S. Rodrigo, and Y. Castro-Diez (1998b), Spatial and temporal patterns of precipitation in Spain for the period 1880–1992, *International Journal of Climatology*, *18*(14), 1557–1574, doi:10.1002/(SICI)1097-0088(19981130)18:14<1557::AID-JOC328>3.0.CO;2-J.

Fernández, J., J. Sáenz, and E. Zorita (2003), Analysis of wintertime atmospheric moisture transport and its variability over Southern Europe in the NCEP Reanalyses, *Climate Research*, *23*(3), 195–215.

Fernández, J., J. P. Montávez, J. Sáenz, J. F. González-Rouco, and E. Zorita (2007), Sensitivity of the MM5 mesoscale model to physical parameterizations for regional climate

studies: Annual cycle, *Journal of Geophysical Research: Atmospheres*, *112*(D4), doi:10.1029/2005JD006649.

Feser, F., B. Rockel, H. von Storch, J. Winterfeldt, and M. Zahn (2011), Regional climate models add value to global model data: A review and selected examples, *Bulletin of the American Meteorological Society*, *92*(9), 1181–1192, doi:10.1175/2011BAMS3061.1.

Foley, A. (2010), Uncertainty in regional climate modelling: A review, *Progress in Physical Geography*, *34*(5), 647–670, doi:10.1177/0309133310375654.

Frías, M. D., S. Herrera, A. S. Cofiño, and J. M. Gutiérrez (2010), Assessing the skill of precipitation and temperature seasonal forecasts in Spain: Windows of opportunity related to ENSO events, *Journal of Climate*, *23*(2), 209–220, doi:10.1175/2009JCLI2824.1.

Gao, B.-C., and Y. J. Kaufman (2003), Water vapor retrievals using Moderate Resolution Imaging Spectroradiometer (MODIS) near-infrared channels, *Journal of Geophysical Research: Atmospheres*, *108*(D13), doi:10.1029/2002JD003023, 4389.

García-Valdecasas Ojeda, M., S. R. Gámiz-Fortis, Y. Castro-Díez, and M. J. Esteban-Parra (2017), Evaluation of WRF capability to detect dry and wet periods in Spain using drought indices, *Journal of Geophysical Research: Atmospheres*, *122*(3), 1569–1594, doi:10.1002/2016JD025683.

Gimeno, L., R. Nieto, R. M. Trigo, S. M. Vicente-Serrano, and J. I. López-Moreno (2010), Where does the Iberian Peninsula moisture come from? An answer based on a Lagrangian approach, *Journal of Hydrometeorology*, *11*(2), 421–436, doi:10.1175/2009JHM1182.1.

Giorgi, F., and X. Bi (2000), A study of internal variability of a regional climate model, *Journal of Geophysical Research: Atmospheres*, *105*(D24), 29,503–29,521, doi:10.1029/2000JD900269.

Gómez-Hernández, M., A. Drumond, L. Gimeno, and R. Garcia-Herrera (2013), Variability of moisture sources in the Mediterranean region during the period 1980-2000, *Water Resources Research*, *49*, 6781–6794, doi:10.1002/wrcr.20538.

Gómez-Navarro, J. J., J. P. Montávez, S. Jerez, P. Jiménez-Guerrero, and E. Zorita (2012), What is the role of the observational dataset in the evaluation and scoring of climate models?, *Geophys. Res. Lett.*, *39*, L24,701, doi:10.1029/2012GL054206.

Gutowski Jr., W. J., Y. Chen, and Z. Ötles (1997), Atmospheric water vapor transport in NCEP-NCAR reanalyses: Comparison with river discharge in the central United States, *Bulletin of the American Meteorological Society*, *78*, 1957–1969, doi:10.1175/1520-0477(1997)078<1957:AWVTIN>2.0.CO;2.

Hastings, D. A., and P. K. Dunbar (1999), Global land one-kilometer base elevation (GLOBE) digital elevation model, documentation, *Key to Geophysical records documentation (KGRD)*, *34*(1.0).

Haylock, M. R., and C. M. Goodess (2004), Interannual variability of European extreme winter rainfall and links with mean large-scale circulation, *International Journal of Climatology*, *24*(6), 759–776, doi:10.1002/joc.1033.

Haylock, M. R., N. Hofstra, A. M. G. Klein Tank, E. J. Klok, P. D. Jones, and M. New (2008), A European daily high-resolution gridded data set of surface temperature and precipitation for 1950–2006, *Journal of Geophysical Research: Atmospheres*, *113*(D20), doi:10.1029/2008JD010201.

Herrera, S., J. M. Gutiérrez, R. Ancell, M. R. Pons, M. D. Frías, and J. Fernández (2012), Development and analysis of a 50-year high-resolution daily gridded precipitation dataset over Spain (Spain02), *International Journal of Climatology*, *32*(1), 74–85, doi:10.1002/joc.2256.

Herrera, S., J. Fernández, and J. M. Gutiérrez (2016), Update of the Spain02 gridded observational dataset for EURO-CORDEX evaluation: assessing the effect of the interpolation methodology, *International Journal of Climatology*, *36*(2), 900–908, doi:10.1002/joc.4391.

Hirschi, M., S. I. Seneviratne, and C. Schär (2006), Seasonal variations in terrestrial water storage for major midlatitude river basins, *Journal of Hydrometeorology*, *7*(1), 39–60, doi:10.1175/JHM480.1.

Huffman, G. J., R. F. Adler, M. M. Morrissey, D. T. Bolvin, S. Curtis, R. Joyce, B. McGavock, and J. Susskind (2001), Global precipitation at one-degree daily resolution from multisatellite observations, *Journal of Hydrometeorology*, *2*(1), 36–50, doi:10.1175/1525-7541(2001)002<0036:GPAODD>2.0.CO;2.

Jerez, S., J. P. Montavez, J. J. Gomez-Navarro, P. Jimenez-Guerrero, J. Jimenez, and J. F. Gonzalez-Rouco (2010), Temperature sensitivity to the land-surface model in MM5 climate simulations over the Iberian Peninsula, *Meteorologische Zeitschrift*, *19*(4), 363–374, doi:10.1127/0941-2948/2010/0473.

Jerez, S., J. P. Montavez, J. J. Gomez-Navarro, P. A. Jimenez, P. Jimenez-Guerrero, R. Lorente, and J. F. Gonzalez-Rouco (2012), The role of the land-surface model for climate change projections over the Iberian Peninsula, *Journal of Geophysical Research: Atmospheres*, *117*(D1), doi:10.1029/2011JD016576.

Jerez, S., J. P. Montavez, J. J. Gomez-Navarro, R. Lorente-Plazas, J. A. Garcia-Valero, and P. Jimenez-Guerrero (2013), A multi-physics ensemble of regional climate change projections over the Iberian Peninsula, *Climate Dynamics*, *41*(7), 1749–1768, doi:10.1007/s00382-012-1551-5.

Jiménez, P. A., and J. Dudhia (2012), Improving the representation of resolved and unresolved topographic effects on surface wind in the WRF model, *J. Appl. Meteor. Climatol.*, *51*, 300–316, doi:10.1175/JAMC-D-11-084.1.

Jiménez, P. A., and J. Dudhia (2013), On the ability of the WRF Model to reproduce the surface wind direction over complex terrain, *Journal of Applied Meteorology and Climatology*, *52*(7), 1610–1617, doi:10.1175/JAMC-D-12-0266.1.

Jiménez, P. A., J. F. González-Rouco, E. García-Bustamante, J. Navarro, J. P. Montávez, J. V.-G. de Arellano, J. Dudhia, and A. Muñoz-Roldan (2010), Surface wind regionalization over complex terrain: Evaluation and analysis of a high-resolution WRF simulation, *J. Appl. Met.*, *49*, 268–287, doi:10.1175/2009JAMC2175.1.

Jiménez-Guerrero, P., J. Montávez, M. Domínguez, R. Romera, L. Fita, J. Fernández, W. Cabos, G. Liguori, and M. Gaertner (2013), Mean fields and interannual variability in RCM simulations over Spain: The ESCENA project, *Climate Research*, *57*(3), 201–220.

Jones, R. G., J. M. Murphy, and M. Noguer (1995), Simulation of climate change over Europe using a nested regional-climate model. I: Assessment of control climate, including sensitivity to location of lateral boundaries, *Quarterly Journal of the Royal Meteorological Society*, *121*(526), 1413–1449, doi:10.1002/qj.49712152610.

Kiladis, G. N., and H. F. Diaz (1989), Global climatic anomalies associated with extremes in the Southern Oscillation, *Journal of Climate*, *2*(9), 1069–1090, doi:10.1175/1520-0442(1989)002<1069:GCAAWE>2.0.CO;2.

Klein Tank, A. M. G., J. B. Wijngaard, G. P. Können, R. Böhm, G. Demarée, A. Gocheva, M. Mileta, S. Pashiardis, L. Hejkrlik, C. Kern-Hansen, R. Heino, P. Bessemoulin, G. Müller-Westermeier, M. Tzanakou, S. Szalai, T. Pálsdóttir, D. Fitzgerald, S. Rubin, M. Capaldo, M. Maugeri, A. Leitass, A. Bukantis, R. Aberfeld, A. F. V. van Engelen, E. Forland, M. Mietus, F. Coelho, C. Mares, V. Razuvaev, E. Nieplova, T. Cegnar, J. Antonio López, B. Dahlström, A. Moberg, W. Kirchhofer, A. Ceylan, O. Pachaliuk, L. V. Alexander, and P. Petrovic (2002), Daily dataset of 20th-century surface air temperature and precipitation series for the European Climate Assessment, *International Journal of Climatology*, *22*(12), 1441–1453, doi:10.1002/joc.773.

Kottek, M., J. Grieser, C. Beck, B. Rudolf, and F. Rubel (2006), World map of the Köppen-Geiger climate classification updated, *Meteorologische Zeitschrift*, *15*(3), 259–263, doi:doi:10.1127/0941-2948/2006/0130.

Leung, L. R., and Y. Qian (2009), Atmospheric rivers induced heavy precipitation and flooding in the western U.S. simulated by the WRF regional climate model, *Geophysical Research Letters*, *36*(3), doi:10.1029/2008GL036445.

Lim, Y.-J., J. Hong, and T.-Y. Lee (2012), Spin-up behavior of soil moisture content over East Asia in a land surface model, *Meteorology and Atmospheric Physics*, *118*(3), 151–161, doi:10.1007/s00703-012-0212-x.

Lionello, P., M. Gacic, D. Gomis, R. Garcia-Herrera, F. Giorgi, S. Planton, R. Trigo, A. Theocharis, M. N. Tsimplis, U. Ulbrich, and E. Xoplaki (2012), Program focuses on climate of the Mediterranean region, *Eos, Transactions American Geophysical Union*, *93*(10), 105–106, doi:10.1029/2012EO100001.

López-Parages, J., and B. Rodríguez-Fonseca (2012), Multidecadal modulation of El Niño influence on the Euro-Mediterranean rainfall, *Geophysical Research Letters*, *39*(2), doi:10.1029/2011GL050049.

Lorenzo, M. N., J. J. Taboada, I. Iglesias, and M. Gómez-Gesteira (2011), Predictability of the spring rainfall in Northwestern Iberian Peninsula from sea surfaces temperature of ENSO areas, *Climatic Change*, *107*(3), 329–341, doi:10.1007/s10584-010-9991-6.

Martens, B., D. G. Miralles, H. Lievens, R. van der Schalie, R. A. M. de Jeu, D. Fernández-Prieto, H. E. Beck, W. A. Dorigo, and N. E. C. Verhoest (2017), GLEAM v3: Satellite-based land evaporation and root-zone soil moisture, *Geoscientific Model Development*, *10*(5), 1903–1925, doi:10.5194/gmd-10-1903-2017.

Miralles, D. G., T. R. H. Holmes, R. A. M. De Jeu, J. H. Gash, A. G. C. A. Meesters, and A. J. Dolman (2011), Global land-surface evaporation estimated from satellite-based observations, *Hydrology and Earth System Sciences*, *15*(2), 453–469, doi:10.5194/hess-15-453-2011.

Montavez, J. P., J. M. Lopez-Romero, S. Jerez, J. J. Gomez-Navarro, and P. Jimenez-Guerrero (2017), How much spin-up period is really necessary in regional climate simulations?, in *EGU General Assembly Conference Abstracts*, vol. 19, p. 15806.

Moseley, S. (2011), From observations to forecasts – Part 12: Getting the most out of model data, *Weather*, *66*(10), 272–276, doi:10.1002/wea.844.

Muñoz-Diaz, D., and F. S. Rodrigo (2004), Spatio-temporal patterns of seasonal rainfall in Spain (1912-2000) using cluster and principal component analysis: comparison, *Annales Geophysicae*, *22*(5), 1435–1448.

Navascués, B., J. Calvo, G. Morales, C. Santos, A. Callado, A. Cansado, J. Cuxart, M. Díez, P. del Río, P. Escribà, O. García-Colombo, J. García-Moya, C. Geijo, E. Gutiérrez, M. Hortal, I. Martínez, B. Orfila, J. Parodi, E. Rodríguez, J. Sánchez-Arriola, I. Santos-Atienza, and J. Simarro (2013), Long-term verification of HIRLAM and ECMWF forecasts over Southern Europe: History and perspectives of Numerical Weather Prediction at AEMET, *Atmospheric Research*, *125*(Supplement C), 20 – 33, doi:https://doi.org/10.1016/j.atmosres.2013.01.010.

Önol, B. (2012), Effects of coastal topography on climate: high-resolution simulation with a regional climate model, *Climate Research*, *52*, 159–174.

Ortiz de Galisteo, J. P., V. Cachorro, C. Toledano, B. Torres, N. Laulainen, Y. Bennouna, and A. de Frutos (2011), Diurnal cycle of precipitable water vapor over Spain, *Quarterly Journal of the Royal Meteorological Society*, *137*(657), 948–958, doi:10.1002/qj.811.

Paredes, D., R. M. Trigo, R. Garcia-Herrera, and I. F. Trigo (2006), Understanding precipitation changes in Iberia in early spring: Weather typing and storm-tracking approaches, *Journal of Hydrometeorology*, *7*(1), 101–113, doi:10.1175/JHM472.1.

Parrish, D. F., and J. C. Derber (1992), The National Meteorological Center's Spectral Statistical-Interpolation Analysis System, *Monthly Weather Review*, *120*, 1747–1763, doi:10.1175/1520-0493(1992)120<1747:TNMCSS>2.0.CO;2.

Peel, M. C., B. L. Finlayson, and T. A. Mcmahon (2007), Updated world map of the Köppen-Geiger climate classification, *Hydrology and Earth System Sciences Discussions*, *4*(2), 439–473.

Peixoto, J., and A. Oort (1992), *Physics of Climate*, New York, NY (United States); American Institute of Physics.

Quadrelli, R., V. Pavan, and F. Molteni (2001), Wintertime variability of mediterranean precipitation and its links with large-scale circulation anomalies, *Climate Dynamics*, *17*(5), 457–466, doi:10.1007/s003820000121.

Reynolds, R. W., T. M. Smith, C. Liu, D. B. Chelton, K. S. Casey, and M. G. Schlax (2007), Daily high-resolution-blended analyses for sea surface temperature, *Journal of Climate*,

20(22), 5473–5496, doi:10.1175/2007JCLI1824.1.

Rios-Entenza, A., and G. Miguez-Macho (2014), Moisture recycling and the maximum of precipitation in spring in the Iberian Peninsula, *Climate Dynamics*, *42*(11), 3207–3231, doi:10.1007/s00382-013-1971-x.

Rios-Entenza, A., P. M. M. Soares, R. M. Trigo, R. M. Cardoso, and G. Miguez-Macho (2014), Moisture recycling in the Iberian Peninsula from a regional climate simulation: Spatiotemporal analysis and impact on the precipitation regime, *Journal of Geophysical Research: Atmospheres*, *119*, 5895–5912, doi:10.1002/2013JD021274.

Rockel, B., C. L. Castro, R. A. Pielke, H. von Storch, and G. Leoncini (2008), Dynamical downscaling: Assessment of model system dependent retained and added variability for two different regional climate models, *Journal of Geophysical Research: Atmospheres*, *113*(D21), doi:10.1029/2007JD009461.

Rodó, X., E. Baert, and F. A. Comín (1997), Variations in seasonal rainfall in Southern Europe during the present century: Relationships with the North Atlantic Oscillation and the El Niño-Southern Oscillation, *Climate Dynamics*, *13*(4), 275–284, doi:10.1007/s003820050165.

Rodríguez-Puebla, C., A. H. Encinas, S. Nieto, and J. Garmendia (1998), Spatial and temporal patterns of annual precipitation variability over the Iberian Peninsula, *International Journal of Climatology*, *18*(3), 299–316, doi:10.1002/(SICI)1097-0088(19980315)18:3<299::AID-JOC247>3.0.CO;2-L.

Rodríguez-Puebla, C., A. H. Encinas, and J. Sáenz (2001), Winter precipitation over the Iberian Peninsula and its relationship to circulation indices, *Hydrology and Earth System Sciences*, *5*, 233–244, doi:10.5194/hess-5-233-2001.

Romero, R., C. Ramis, and J. Guijarro (1999), Daily rainfall patterns in the Spanish Mediterranean area: An objective classification, *International Journal of Climatology*, *19*, 95–112, doi:10.1002/(SICI)1097-0088(199901)19:1<95::AID-JOC344>3.0.CO;2-S.

Rubel, F., K. Brugger, K. Haslinger, and I. Auer (2017), The climate of the European Alps: Shift of very high resolution Köppen-Geiger climate zones 1800-2100, *Meteorologische Zeitschrift*, *26*(2), 115–125, doi:10.1127/metz/2016/0816.

Rummukainen, M. (2010), State-of-the-art with regional climate models, *Wiley Interdisciplinary Reviews: Climate Change*, *1*(1), 82–96, doi:10.1002/wcc.8.

Sáenz, J., C. Rodríguez-Puebla, J. Fernández, and J. Zubillaga (2001), Interpretation of interannual winter temperature variations over Southwestern Europe, *Journal of Geophysical Research: Atmospheres*, *106*(D18), 20,641–20,651, doi:10.1029/2001JD900247.

Sein, D. V., N. V. Koldunov, J. G. Pinto, and W. Cabos (2014), Sensitivity of simulated regional Arctic climate to the choice of coupled model domain, *Tellus A: Dynamic Meteorology and Oceanography*, *66*(1), 23,966, doi:10.3402/tellusa.v66.23966.

Skamarock, W. C., J. B. Klemp, J. Dudhia, D. O. Gill, D. M. Barker, M. G. Duda, X.-Y. Huang, W. Wang, and J. G. Powers (2008), A description of the advanced research WRF version 3, *NCAR Technical Note NCAR/TN-475+STR*, doi:10.5065/D68S4MVH.

Snider, J. B. (2000), Long-term observations of cloud liquid, water vapor, and cloud-base temperature in the North Atlantic Ocean, *Journal of Atmospheric and Oceanic Technology*, *17*, 928–939, doi:10.1175/1520-0426(2000)017<0928:LTOOCL>2.0.CO;2.

Soares, P. M. M., R. M. Cardoso, P. M. A. Miranda, J. de Medeiros, M. Belo-Pereira, and F. Espiritu-Santo (2012), WRF high resolution dynamical downscaling of ERA-Interim for Portugal, *Clim. Dyn.*, *39*, 2497–2522, doi:10.1007/s00382-012-1315-2.

Soares, P. M. M., R. M. Cardoso, J. a. J. Ferreira, and P. M. A. Miranda (2015), Climate change and the Portuguese precipitation: ENSEMBLES regional climate models results, *Climate Dynamics*, *45*, 1771–1787, doi:10.1007/s00382-014-2432-x.

Sousa, P. M., R. M. Trigo, D. Barriopedro, P. M. M. Soares, A. M. Ramos, and M. L. R. Liberato (2017), Responses of European precipitation distributions and regimes to different blocking locations, *Climate Dynamics*, *48*, 1141–1160, doi:10.1007/s00382-016-3132-5.

Stacke, T., and S. Hagemann (2016), Lifetime of soil moisture perturbations in a coupled land–atmosphere simulation, *Earth System Dynamics*, *7*(1), 1–19, doi:10.5194/

esd-7-1-2016.

Trenberth, K. E., and C. J. Guillemot (1998), Evaluation of the atmospheric moisture and hydrological cycle in the NCEP/NCAR reanalyses, *Climate Dynamics*, *14*(3), 213–231, doi:10.1007/s003820050219.

Trenberth, K. E., L. Smith, T. Qian, A. Dai, and J. Fasullo (2007), Estimates of the global water budget and its annual cycle using observational and model data, *Journal of Hydrometeorology*, *8*(4), 758–769, doi:10.1175/JHM600.1.

Trigo, I. F., T. D. Davies, and G. R. Bigg (1999), Objective climatology of cyclones in the Mediterranean region, *Journal of Climate*, *12*(6), 1685–1696, doi:10.1175/1520-0442(1999)012<1685:OCOCIT>2.0.CO;2.

Tullot, I. F. (2000), *Climatología de España y Portugal*, vol. 76, Universidad de Salamanca.

Tustison, B., D. Harris, and E. Foufoula-Georgiou (2001), Scale issues in verification of precipitation forecasts, *Journal of Geophysical Research: Atmospheres*, *106*(D11), 11,775–11,784, doi:10.1029/2001JD900066.

Ulazia, A., J. Sáenz, and G. Ibarra-Berastegui (2016), Sensitivity to the use of 3DVAR data assimilation in a mesoscale model for estimating offshore wind energy potential. A case study of the Iberian northern coastline, *Applied Energy*, *180*(Supplement C), 617 – 627, doi:https://doi.org/10.1016/j.apenergy.2016.08.033.

van den Besselaar, E. J. M., M. R. Haylock, G. van der Schrier, and A. M. G. Klein Tank (2011), A European daily high-resolution observational gridded data set of sea level pressure, *Journal of Geophysical Research: Atmospheres*, *116*(D11), doi:10.1029/2010JD015468.

Vérant, S., K. Laval, J. Polcher, and M. D. Castro (2004), Sensitivity of the continental hydrological cycle to the spatial resolution over the Iberian Peninsula, *Journal of Hydrometeorology*, *5*(2), 267–285, doi:10.1175/1525-7541(2004)005<0267:SOTCHC>2.0.CO;2.

Vicente-Serrano, S. M., R. M. Trigo, J. I. López-Moreno, M. L. R. Liberato, J. Lorenzo-Lacruz, S. Beguería, E. Morán-Tejeda, and A. E. Kenawy (2011), Extreme winter precipitation in the Iberian Peninsula in 2010: Anomalies, driving mechanisms and future projections, *Climate Research*, *46*(1), 51–65.

Vicente-Serrano, S. M., C. Azorin-Molina, A. Sanchez-Lorenzo, E. Morán-Tejeda, J. Lorenzo-Lacruz, J. Revuelto, J. I. López-Moreno, and F. Espejo (2014), Temporal evolution of surface humidity in Spain: Recent trends and possible physical mechanisms, *Climate Dynamics*, *42*, 2655–2674, doi:10.1007/s00382-013-1885-7.

Wang, J.-J., R. F. Adler, G. J. Huffman, and D. Bolvin (2014), An updated TRMM composite climatology of tropical rainfall and its validation, *Journal of Climate*, *27*(1), 273–284, doi:10.1175/JCLI-D-13-00331.1.

Yeh, P. J.-F., and J. S. Famiglietti (2008), Regional terrestrial water storage change and evapotranspiration from terrestrial and atmospheric water balance computations, *Journal of Geophysical Research: Atmospheres*, *113*(D9), doi:10.1029/2007JD009045.

Zheng, D., R. Van Der Velde, Z. Su, J. Wen, and X. Wang (2017), Assessment of Noah land surface model with various runoff parameterizations over a Tibetan river, *Journal of Geophysical Research: Atmospheres*, *122*(3), 1488–1504, doi:10.1002/2016JD025572.

Zveryaev, I. I., J. Wibig, and R. P. Allan (2008), Contrasting interannual variability of atmospheric moisture over Europe during cold and warm seasons, *Tellus A*, *60*(1), 32–41, doi:10.1111/j.1600-0870.2007.00283.x.

Table 3. Spatial quantile-based analysis of the correlations obtained for precipitation in both WRF experiments and ERAI with the validation datasets: EOBS, ECA&D, GPCP and TRMM.

Experiment	**q97.5**	**q95**	**q75.**	**q50**	**q25**	**q5**	**q2.5**
EOBS-N	0.71	0.68	0.59	0.53	0.48	0.36	0.32
EOBS-D	0.76	0.74	0.68	0.64	0.61	0.55	0.53
EOBS-ERA	0.76	0.74	0.68	0.63	0.58	0.52	0.49
ECA&D-N	0.59	0.57	0.49	0.44	0.39	0.31	0.29
ECA&D-D	0.69	0.67	0.57	0.53	0.50	0.46	0.45
ECA&D-ERA	0.60	0.60	0.53	0.50	0.45	0.39	0.38
GPCP-N	0.58	0.57	0.48	0.39	0.31	0.23	0.21
GPCP-D	0.60	0.58	0.53	0.46	0.41	0.32	0.29
GPCP-ERA	0.58	0.58	0.52	0.47	0.41	0.33	0.31
TRMM-N	0.57	0.54	0.44	0.36	0.28	0.20	0.18
TRMM-D	0.63	0.60	0.53	0.48	0.42	0.32	0.30
TRMM-ERA	0.62	0.60	0.55	0.48	0.42	0.35	0.33

Table 4. Same as Table 3 but for bias (mm/day).

Experiment	**q97.5**	**q95**	**q75.**	**q50**	**q25**	**q5**	**q2.5**
EOBS-N	0.59	0.48	0.18	-0.05	-0.39	-1.38	-1.84
EOBS-D	0.88	0.71	0.31	0.12	-0.15	-0.72	-1.05
EOBS-ERA	0.93	0.71	0.16	-0.04	-0.25	-0.59	-0.67
ECA&D-N	0.89	0.68	0.32	0.20	-0.10	-0.90	-0.99
ECA&D-D	1.02	0.77	0.43	0.28	0.09	-0.17	-0.23
ECA&D-ERA	1.09	1.08	0.29	0.00	-0.17	-0.38	-0.42
GPCP-N	1.13	1.06	0.77	0.49	-0.03	-1.42	-2.01
GPCP-D	1.25	1.18	0.87	0.63	0.27	-0.73	-1.19
GPCP-ERA	1.09	0.93	0.63	0.43	0.22	-0.25	-0.55
TRMM-N	0.73	0.51	-0.14	-0.45	-0.88	-2.70	-3.23
TRMM-D	0.86	0.64	-0.05	-0.33	-0.63	-1.81	-2.31
TRMM-ERA	0.90	0.41	-0.21	-0.51	-0.74	-1.66	-1.82

Figure 19. Top: Domain of both simulations marked with grey dots. The mask defined for the IP is plotted in red. That was the area used for verification. Bottom left: topography of the IP taken from GLOBE dataset (at 1 km resolution; [*Hastings and Dunbar*, 1999]) and bottom right: topography as represented in our WRF simulations (15 km resolution).

Figure 20. Taylor diagrams showing the standard deviation, r and RMSE results for N and D experiments and ERAI compared to radiosonde data (coloured in red, green and orange respectively). The small dots represent the results for each time series created using the bootstrap technique, while the big dots correspond to the results obtained from the full sample of observed radiosonde data.

Figure 21. Correlation for both WRF simulations and ERAI compared to IWV data collected by MODIS aboard Aqua and Terra satellites. The spatial average of the points included in the IP is presented in the right bottom corner of the map.

Figure 22. Same as Figure 21, but for bias (mm).

Figure 23. Precipitation correlation maps between EOBS dataset for both WRF simulations and ERA (shaded). Coloured circles represent the correlation of 21 stations selected from ECA&D. The mean r values for EOBS and ECA&D datasets are presented in the right bottom corner of the maps.

Figure 24. Same as Figure 23, but for bias (mm/day).

Figure 25. Eliminated points from the validation of evaporation because of the lack of ability to simulate observed evaporation by Noah Land Surface Model depending on their land uses. All urban and built-up grid points (orange) were deleted, but also some points representing evergreen broadleaf forest (magenta), mixed forests (cyan), open shrublands (coral) and croplands (green).

Figure 26. Evaporation correlation maps between GLEAM (version 3.0b) for both WRF simulations and ERAI. All of the problematic points presented in Figure 25 are eliminated from this validation. The mean r values are presented in the right bottom corner of the maps.

Figure 27. Same as Figure 26 but for bias (mm/day).

Figure 28. Areal mean evaporation simulated by different datasets and experiments for 2010-2014. GLEAM v3.0b in blue, GLEAM v3.0c in magenta, the N experiment in red, the D experiment in green and ERAI in orange.

Figure 29. Areal mean of the precipitation (MArealRAIN), the evaporation (MArealEVAP), the divergence of moisture flux (MArealDivQ), the tendency of the IWV (DerivQ) and the residual according to the experiment: ERAI in orange, the N experiment in red and the D experiment in green (mm/day).

Figure 30. Areal mean of the residual over the IP according to the D experiment stratified by season (winter DJF, spring MAM, summer JJA, autumn SON) and hour (00 UTC, 06 UTC, 12 UTC and 18 UTC in blue, red, green and orange respectively).

Figure 31. Left: Areal mean over the IP of the analysis minus background of the specific humidity at 2m (1×10^{-3} kg/kg) according to the season (winter DJF, spring MAM, summer JJA, autumn SON) and hour (00, 06, 12 and 18 UTC in blue, red, green and orange respectively). Right: Spatial distribution of the analysis minus background during summer at 12 UTC (top) and 18 UTC (bottom).

Figure 32. Mean daily evaporation (mm/day) simulated by the D experiment over the IP for winter (left) and summer (right). The mean value of the evaporation over the IP is presented in the right bottom corner of the maps.

Figure 33. Accumulated annual precipitation (mm) over the IP taken from the Spanish Meteorological Agency atlas [*AEMET*, 2011] for 1971-2000 (left), compared to those from the D experiment (top right) and from ECA&D over EOBS (bottom right).

Figure 34. Mean daily IWV (mm) simulated by the D experiment over the IP for winter (top left), spring (top right), summer (bottom left) and autumn (bottom right).

Figure 35. Transboundary moisture fluxes analysis at 00 UTC (top left), 06 UTC (top right), 12 UTC (bottom left) and 18 UTC (bottom right) during winter. The reference bar is labelled at 6.5 Pg/month. The green bars represent an inland flux, while the blue bars refer to an outward flux.

Figure 36. Same as Figure 35 but for summer.